Patient-Derived Organoids Recapitulate Intrinsic Immune Landscapes and Progenitor Populations of Glioblastoma.

Authors: Fumihiro Watanabe[1,2#], Ethan W. Hollingsworth[1,2,10#], Jenna M. Bartley[3], Lauren Wisehart[1], Rahil Desai[1], Annalisa M. Hartlaub[4], Mark E. Hester[4,5,6], Paula Schiapparelli[7], Alfredo Quiñones-Hinojosa[7], and **Jaime Imitola[1,2*]**

Affiliations:

[1]Laboratory of Neural Stem Cells and Functional Neuroimmunology Genetics, [2]Departments of Neuroscience, Neurology, Genetics and Genome Sciences, UConn Health, Farmington, CT, 06030, USA, [3]Center on Aging UConn Health, Farmington, CT, 06030, USA. [4]The Steve and Cindy Rasmussen Institute for Genomic Medicine, [5]Department of Pediatrics, The Ohio State University College of Medicine, Columbus, Ohio, USA; [6]Department of Neuroscience, The Ohio State University Wexner Medical Center, Columbus, Ohio, USA. [7]Brain Tumor Stem Cell Laboratory, Department of Neurosurgery, Mayo Clinic, Jacksonville, Florida, 32224, USA.

[10]Present address: Medical Scientist Training Program, Department of Developmental and Cell Biology, University of California Irvine, Irvine, California 92697, USA.

***Corresponding author email: imitola@uchc.edu**

#These authors contributed equally to this work

Keywords: Organoids, Glioblastoma stem cells, glioma intrinsic programs, interferon, HOPX, SATB2

Running title: Intrinsic molecular programs of GBM organoids

Words: 7259

Figures: 6

Supplementary Figures: 10

Tables: 14

Glioblastoma stem cells (GSCs) are highly self-renewing, resistant to therapy, and are able to form lethal tumors[1,2]. Tumor organoids have been developed to study tumor evolution[1-4], and while GSCs can form organoids for glioblastoma multiforme, our understanding of their intrinsic immune, metabolic, genetic, and molecular programs is limited. To address this, we deeply characterized GSC-derived GBM organoids using a modified protocol (GBMOsm) from several patient-derived GSCs and found they develop into complex 3D tissues with unique self-organization, cancerous metabolic states, and burdensome genetic landscapes. We discovered that GBMOsc recapitulate the presence of two important cell populations thought to drive GBM progression, SATB2^{+} and HOPX^{+} progenitors. Despite being devoid of immune cells, transcriptomic analysis across GBMOsc revealed an immune-like molecular program, enriched in cytokine, antigen presentation and processing, T-cell receptor inhibitors, and interferon genes. We determined that SATB2^{+} and HOPX^{+} populations contribute to this immune and interferon landscape in GBM in vivo and GBMOsm. Our work deepens our understanding of the intrinsic molecular and cellular architecture of GSC-derived GBMO and defines a novel GBMOsc intrinsic immune-like program.

Introduction

Glioblastoma multiforme (GBM) remain one of the most lethal cancers worldwide[5]. One prevailing model of GBM posits that tumors originate and recur from glioblastoma stem cells (GSCs)[5-7]. Like other stem cells, GSCs have increased self-renewal capacity and exhibit a progenitor-like state, but differ in their pathological properties, including increased survival, aneuploidy, oncogenesis, and resistance to therapy. Beyond the cell-autonomous component of GSCs and maturing cancer cells, GBM evolve by forming a tumor microenvironment (TME). That is, a collection of non-tumoral cells, including vascular, immune, and mesenchymal cells, that permit angiogenesis, local immunosuppression (thereby facilitating tumor cell proliferation), and migration and invasion into normal tissue, which altogether leads to explosive tumor growth. This TME crosstalk shapes the intrinsic properties of the developing tumor itself. One important example, for instance, is that GBM cells regulate infiltrating cell types according to their own mutational landscape[8], as well as their own glioma-intrinsic gene expression programs[9]. Thus, how exactly an initial cluster of GBM cells can evolve and co-opt the TME to favor tumor promotion remains a fundamental unanswered question with important clinical and therapeutic implications.

Preclinical models have consisted mainly of genetically engineered mouse models or human tumor-derived cell lines propagated in either two-dimensional (2D) cultures or as patient-derived xenografts (PDXs) in mice[10,11]. There has been a growing interest in glioblastoma organoids[4,12-16]. Organoids are defined as 3D *in vitro* tissue-like constructs derived from isolated stem cells which mimic their corresponding *in vivo* organ. Among the several models of GBM organoids [4,12-16] is one derived from intact microscopic pieces of tissue from surgically resected tumors termed (GBO). This model offers the advantage of closely replicating its native tumor, since the tissue has not undergone major alterations other than being placed in defined cultures, and thus could be very useful for chemical screenings of potential therapeutic compounds. However, this model is less suitable for studying the initial GBM intrinsic program and early self-organization of GBM since the tumor is already organized *in vivo* and retains its complete TME, with infiltrating immune and vascular cells[14]. Therefore, it is challenging to experimentally distinguish the intrinsic human GBM from the stroma laden with diverse cells. Moreover, by the time GBM are usually detected, tumor and microenvironment interactions are long established. An alternative GBM organoid model is one derived from GSCs isolated from a patient's resected GBM surgical tissue, which are used to generate GBM organoids, recapitulating aspects of GBM tissue and organization[15]. However, it relies on the addition of exogenous growth factors during organoid formation and differentiation, which may favor unwanted proliferation of GSCs and clonal selection rather than inducing the initial events of 3D tissue-like tumor formation seen in regular iPSCs and NSCs-derived organoids and making comparison difficult since these organoids don't require growth factors during the organoid formation stage.

In this study, applying an improved protocol, we performed a comprehensive, integrative

85 characterization of GBM organoids generated from several patient-derived GSCs, we termed GBMOsm
86 (GSC-derived GBM Organoid derived from GBM Stem Cells with Modified Protocol), Henceforth, GBMOs.
87 We specifically examined GBMO microanatomy, progenitor diversity, mutational and transcriptomic
88 landscapes, and their intrinsic gene expression programs, especially as they relate to GBM *in vivo*. Our work
89 advances our understanding of the intrinsic cellular and molecular features of GSC-derived GBMO,
90 including the identification of novel progenitor populations and immune gene signatures.
91

92 **Results**

93

94 **Patient-derived GSCs self-organize into 3D tumor tissue-like structures.**

95 GBM have unique spatial and temporal characteristics, with tissue-like domains and cellular diversity[15]. GSCs
96 are also thought to underlie glioma origin, initiation, evolution, and therapy resistance. Studying GSCs is usually done
97 by injecting these cells into mice brains, as a xenotransplant into a immunosuppressed host. This approach is less
98 suitable to dissect autologous neuroimmune interactions[17] seen in neuroinflammation[5,18] and in brain cancer[7].
99 Previously, we showed the intrinsic ability of normal neurospheres to form through aggregation, a complex tissue-
100 like construct, resulting in self-organization, and progenitor diversity that we called NEDAS[19]. Furthermore, we have
101 shown that neurospheres have an intrinsic immune program, which express T cell co-stimulatory molecules and
102 chemokine receptors that are functional during neuroinflammation in multiple sclerosis models[20-22]. Thus, we
103 hypothesized that GSCs spheres like NSCs spheres may share developmental potential characteristics. A previous
104 report showed GSCs are able to form organoids, but the study of their intrinsic properties including their
105 neuroimmune phenotype is unknown[15].

106 To expand on these efforts, we cultured GSC-derived tumorspheres from patients who underwent GBM
107 resection and then generated GBMOs, that are proven to be GSCs *in vivo* and *in vitro* in prior work.[23-26]
108 (**Supplementary Figure 1a-c, Supplementary Table 1**). Prior GSC-derived organoids were maintained at all times
109 under conditions of EGF/FGF. Typically organoids are maintained in defined medium without added growth factors
110 from organoid generation, we favored this method to allow comparison with control organoids. We embedded GSCs
111 in Matrigel and generated GBMOs with a 94% success rate (n=314 organoids from 6 GSC lines after 4 weeks in
112 culture). **Supplementary Fig. 1f, 2a-b** The organoids reached sizes 20-fold larger than GSCs grown as "tumorspheres"
113 (a cancer cell aggregate;). (**Supplementary Fig. 2a,b).** GSCs aggregated and integrated into a uniform tissue
114 architecture. Pathology comparison of GBMOs and parental tumors showed proliferative and quiescent/necrotic
115 compartments, in addition to the presence of pseudopalisading cells in selected tumor-organoid pairs

116 (**Supplementary Fig. 1d,e**). For instance, GBMO-965 remained sparsely cellular with syncytia-like formations while
117 GBMO-1201 retained its multicellularity with fibrils and occasional highly chromatic nuclei. These findings are
118 consistent with recent work indicating that GBM organoids derived from intact tissue (GBOs) reproduce features of
119 their parental tumors[15]. These findings demonstrated that GSCs can form 3D organoids without added growth factors
120 allowing us to perform an in depth-phenotypic characterization and comparisons using similar cultures protocols for
121 iPSCs (iPSCO) and organoids derived from NSCs (NSCO).

122

123 **Patient-derived GBMO host distinct microenvironments and progenitor diversity mimicking GBM biology**

124

125 Next, we compared GBMO self-organization to non-tumoral, age-matched organoids derived from healthy
126 neurospheres from H9-derived human neural stem cells (NSCO)[19] (**Fig.1a)**. We also used cerebral organoids derived
127 from human iPSCs (iPSCO), which we and others have shown recently to model the stereotypical architecture of the
128 developing brain with self-organized progenitor niches[27,28] and cortical layering. GBMO, NSCO, and iPSCO, all
129 maintained in Matrigel and growth factor-free culture conditions, uniformly expressed the human NSC marker,
130 vimentin (VIM)[29]. These organoids were composed of segregated areas of proliferation, marked by Ki-67 (Ki-67$^+$),
131 apoptosis by activated-caspase-3 (A-Cas$^+$), and quiescent/stressed cells by activating transcription factor 4 (ATF4$^+$),
132 albeit to a lesser extent in NSCO (**Fig. 1b-f and Supplementary Fig. 3a, b**). By contrast, GSCs cultured as tumorspheres
133 in EGF/FGF lacked any such organization (**Supplementary Fig. 2a, b**). We quantified Ki-67$^+$ and A-Cas$^+$ layer thickness
134 among GBMO and found GBMO-30 contained marked overlap while the others exhibited a clear delineation of
135 proliferating cells from the outside surface and apoptotic and quiescent cells from the inner core (**Fig. 1c-e**). As
136 organoids expand, their inner core experiences a reduction in oxygenation due to diffusion limits[15]. To determine
137 hypoxic gradients in GBMOs, we stained for the BCL-2 interacting protein-3 (BNIP3), a protein downstream of
138 hypoxia-inducible factor 1α (HIF-1α) and a marker for hypoxia[30]. We found increased cytoplasmic and nuclear BNIP3
139 expression inside GBMO compared to their surfaces, as shown by quantitative confocal intensity profile
140 measurements (**Fig. 1b and Supplementary Fig. 3c, d, e, f)**. Collectively, these data indicate that all examined GBMO
141 hosted microenvironments for apoptosis, proliferation, hypoxia, and cellular stress as seen in GBM *in vivo*.

142 To determine the functional basis for the expression of the radial glia marker VIM in GBMOs, we stained for
143 the phosphorylated form (p-VIM), a marker for radial glia division. Notably, we found a population of p-VIM$^+$ radial
144 glia-like tumor cells undergoing mitosis in the proliferating layers of GBMO (**Supplementary Fig. 3g**). We confirmed
145 their identity by staining for homeodomain-only protein homeobox (HOPX), a transcriptional regulator and marker

146 for outer radial glia (oRG) in normal human neurodevelopment. Unlike their stereotypical localization to the outer
147 subventricular zone (SVZ) in iPSCO, we observed multiple HOPX$^+$ cells scattered throughout the outer edge of
148 GBMOs, some with characteristic polarity and elongated processes (**Fig. 1g**). This oRG-like population in GBM has
149 been recently described as invasive GBM cells with stem cell and migratory properties *in vivo*. Altogether, these data
150 demonstrate that GBMO derived from GSCs are capable of replicating the pathological oRG-like cell population
151 observed in GBM *in vivo* and GBM tissue *ex vivo*[14,31,32].

152

153 The identification of these oRG-like tumor cells, together with the known ability of GSCs to co-opt
154 developmental programs to direct tumorigenesis[33], prompted us to examine the molecular diversity of progenitor
155 markers in GBMO. We performed an analysis of well-defined neural progenitor markers in all GBMO and compared
156 them with their expression levels reported in GBM *in vivo* (**Fig 2b**). In iPSCO, as expected, we observed well-defined
157 SOX2$^+$ ventricular zone (VZ) and SVZ-like areas adjacent to cortical plate-like areas containing CTIP2$^+$ cells, a marker
158 for early born cortical neurons[27] (**Fig. 1h**). In contrast, we did not observe CTIP2$^+$ cells in any GBMO, mirroring its low
159 expression in GBM *in vivo* (**Fig. 2b**). Though unsurprisingly absent in GBM-30, which is characterized by the
160 mesenchymal phenotype *in vivo*[24,25,34], SOX2$^+$ cells were variable among patient-derived lines and dispersed
161 throughout the layers of GBMO (**Fig. 1h**). We stained for additional lineage markers, including PAX6; the intermediate
162 cell marker TBR2; deep-layer neuron markers, SATB2 and TBR1; and Cajal-Retzius cell marker, REELIN (**Fig, 2a**). Unlike
163 iPSCO, where cells were stereotypically located, these cell type markers showed disorganized expression scattered
164 throughout GBMO. Marker expression intensity largely reflected what has been reported in GBM *in vivo*. For
165 instance, SATB2 (**Fig. 2a-middle**), a bona-fide marker for GSCs that was recently found to be a driver for GBM
166 growth[35], was highly expressed in GBMO compared to NSCO, while TBR1 was expressed in all GBMOs (**Fig. 2a-upper**).
167 Collectively, these results indicate that GSCs form organoids that not only contain proliferative, apoptotic, and
168 quiescent niches that vary in their relative size, but also reactivate a progenitor program like GBM *in vivo*, including
169 the oRG-like HOPX$^+$ and SATB2$^+$ cancer stem cell populations (**Fig. 2b,c**).

170

171 **Genomic architecture of GBMO reflect alterations found in GBM**

172 Thus far, detailed genomic and mutational analyses of GSC-derived GBMO have not been performed. *In vivo*,
173 GBM present with a high degree of aneuploidy, copy number changes, and somatic mutations[36]. To evaluate the
174 genetic landscape of GBMO, we performed targeted massively parallel DNA sequencing (TMPDS) and large-scale
175 chromosomal copy-number variation (CNV) analysis of all patient-derived GBMOs[37] and NSCO[19] that were cutured

176 simultenously with identical culture conditions **(Fig.3a).** CNV analysis revealed a greater number of CNVs across all
177 GBMOs, relative to NSCO. These included sizable amplifications in chromosome 7 and deletions in chromosome 10,
178 which were shared among GBMO-1201, GBMO-965, and GBMO-640 and have been frequently reported in GBM (**Fig.**
179 **3b and Supplementary Table 4**). We next employed TMPDS to identify somatic mutations in GBMO and NSCO. From
180 a panel of 407 cancer-related genes, we identified 32 somatic mutations in GBMO-30, nine in GBMO-965, seven in
181 GBMO-1201, and five in GBMO-640 while NSCO harbored five non-damaging mutations (**Fig. 3c and Supplementary**
182 **Table 5**). Of the genes mutated in GBMO, the majority (GBMO-30, 70%; GBMO-965, 89%; GBMO-1201, 71%; GBMO-
183 640, 60%) are mutated in native GBM *in vivo*[38]. Moreover, whereas four of the five mutated genes in NSCO are
184 tolerated missense (SIFT score <0.05) (**Fig. 3d**), most GBMO mutations are predicted to be damaging, frame-shifting,
185 or protein-truncating (**Fig. 3c-e**). GBMO-30, in particular, was composed of the most damaging frame-shift and
186 nonsense mutations (**Fig. 3d,f**).This mutational spectrum, consisting of nonsynonymous mutations with an increased
187 frequency of G>A/C>T transversions, is also in accord with that of GBM[39]. Functionally, many of the GBMO-detected
188 mutations affect genes commonly mutated in GBM, including *IDH2*, *TP53*, and *PTEN*, the chromatin modifiers,
189 *CREBBP*, *SETD2*, *KDM6A*[40], and *ATRX*, with the latter involved in impaired non-homologous end joining and found in
190 30% of GBM[41]. Altogether, these data demonstrate that GBMO mimic the mutational landscape commonly seen in
191 GBM (**Fig. 3e,f and Supplementary Table 5**).

192

193 **Molecular landscapes of GBMO reflect metabolic and molecular alterations found in GBM**

194 Next, we performed gene expression analysis in GBMO and NSCO in which both organoids were
195 maintained in identical culture conditions. Principal component analysis of GBMO global transcriptomes
196 indicated similarity between GBMO-1201 and GBMO-965, as well as between NSCO and GBMO-640, while
197 GBMO-30 clustered by itself, suggesting a distinct expression state from the others (**Fig. 3g**). Using the
198 classifier gene sets[42], we then calculated subtype scores and found that GBMO-965, -640, and -1201 are
199 most aligned with the classical subtype (**Fig. 3h**). GBMO-30 expressed predominantly mesenchymal subtype
200 genes, in agreement with its absence of SOX2. Consistent with the high metabolic profile of GBM,
201 differential expression analysis indicated that all GBMO except GBO-640 are driven by the Warburg Effect
202 where aerobic glycolysis and lactate fermentation predominate (**Fig. 3i**). Additionally, we found that GBMO
203 showed elevated methionine cycle gene expression, a recently uncovered metabolic pathway essential for
204 glioma stem cells[43](**Fig. 3j**). Seahorse metabolic analysis confirmed elevated levels of mitochondrial ATP
205 (Mito ATP) and glycolytic ATP (Glyco ATP) production rates in GBMO compared to NSCO (**Fig. 3k-m).**
206

207 To better understand GBM gene programs on a global scale, we determined differential expression
208 (DE; defined as $\log_2(FC) \pm 2$ and FDR-adjusted p-value < 0.05) between GBMO and NSCO. We identified

209 1743 DE genes (DEGs) across GBMO (**Fig. 4a-left and Supplementary Table 6**); unsupervised hierarchal
210 clustering of these DEGs yielded five gene clusters of interest (**gene ontology, Fig.4a-right**). The largest
211 cluster, containing genes almost exclusively upregulated in GBMO, surprisingly was enriched for immune
212 signaling genes associated with immunity, interferon genes (*IFITM1*, *STAT1*, *OAS1*, *IRF9*, *IRF3, IRF1, HLA,*
213 *NFKB1*), cytokines (*IL6*), as well as hallmark processes of cancer (*IDH1)* and *(MEF/ELF4),* a transcription
214 factor associated with stemness in GBM (**Fig. 4a, blue columns**). The next largest cluster included genes
215 upregulated in GBMO-1201 and -965, and NSCO, suggesting both utilize similar chromatin and Wnt
216 signaling pathways (**Fig. 4a, red columns**). Finally, GBMO-30 was enriched for cell cycle genes, like *ASPM*
217 and *TOP2A*, suggesting it to be the most mitotically active and supporting its highly malignant profile (**Fig**
218 **4a, green column**).
219 In contrast, gene ontology (GO) and pathway analysis of NSCO-specific clusters indicated
220 enrichment for molecules belonging to human neurodevelopment, consistent with the upregulation of
221 known neurogenic genes (*DCX*, *STMN2*, and *NRXN1*) in NSCO (**Fig. 4a, orange column**). We confirmed the
222 diversity of expression of genes proposed to be involved in GBM[25] which showed heterogenous, but
223 increased expression in all GBMO compared to NSCOs, suggesting that each organoid may have different
224 gene networks that participate in driving their growth (**Supplementary Fig. 4a-b**). We confirmed these
225 transcriptomic results by quantitative polymerase chain reaction (qPCR) in GBMO-30 (**Supplementary Fig.**
226 **4c).**
227 Next, we investigated if the upregulated genes in GBMO are similarly overexpressed in primary
228 gliomas and GBM by leveraging publicly available bulk sequencing data of patient samples from The Cancer
229 Genome Atlas (TCGA) (**Supplementary Fig. 5a**). Evaluation of the topmost upregulated genes in each GBMO
230 by glioma subtype in TCGA revealed a bias toward GBM, opposed to astrocytomas and oligodendrogliomas
231 (17 DE in GBM; 10 DE in Astro; 9 DE in Oligo) (**Supplementary Fig. 5b**). Moreover, examination of these
232 genes by GBM subtype in the TCGA database supported our mesenchymal and classical subtype findings
233 (18 DE in Mes; 19 DE in Cla; 10 in Pro) (**Fig. 3h and Supplementary Fig. 5c**). Since we found distinct regions
234 of proliferation, apoptosis, hypoxia, and quiescent cells in GBMO, we next asked how genes upregulated in
235 GBMOsc reflect gene expression of different GBM histological compartments. To do this, we used the IVY
236 Glioblastoma Atlas Project (Ivy GAP), an RNA sequencing dataset of microdissected GBM structures from 37
237 patients. While NSCO genes localized to the leading edge, which is known to contain endogenous neural
238 and neoplastic tissue, we observed genes upregulated in GBMOsc to be highly expressed in the leading
239 edge, hyperplastic vessel, and microvascular proliferative domains (**Supplementary Fig.6 and**
240 **Supplementary Table 7**). Altogether, these results suggest that GSC-derived GBMO reproduce
241 histopathological phenotypes, mutational landscape, expression state, and molecular microanatomy of
242 GBM *in vivo*, providing an opportunity to study the functional relevance of intrinsic molecular pathways at
243 critical stages of GBMO evolution.
244
245 **GBMO intrinsic gene expression is enriched for unique glia immune-like molecular programs.**
246 One unique advantage of our GBMOsc system is its lack of stromal cells compared to other GBM

247 organoid platforms, which harbor endothelial and immune cells[15]. We leveraged this feature to define an
248 intrinsic glial genetic program, representative of a pre-angiogenic state. To do this, we analyzed the top
249 one-third of expressed genes in each GBMO and focused on the convergence of these genes between all
250 GBMOsc lines to find a shared molecular program. We found 1,974 genes (**Fig. 4c**), which we henceforth
251 refer to as the GBMOsc-intrinsic program (**Fig. 4d**). To gain insights into the functional architecture of this
252 program, we performed pathway and ontology enrichment analyses. The GBMOsc-intrinsic program
253 exhibited enrichment for pathways known to be dysregulated in cancer, such as p53, integrin signaling,
254 glycolysis, and angiogenesis. Gene ontology analysis, on the other hand, highlighted a substantial
255 enrichment for genes involved in immune signaling, consistent with our previous analysis of DEGs (**Fig. 4d**
256 **and Fig. Supplementary Fig. 7a**). Reasoning that GBM cells may engage in immune interaction with T cells,
257 we next examined the expression of costimulatory/inhibitory pathways[44,45]. GBMOsc showed increased
258 expression of *PD-L1* in GBMO-640 and GBMO-1201, and *PD-L2* in GBM-30. We also observed elevated
259 expression of MHC class I genes in all GBMOsc, especially GBMOsc-30 (**Fig. 4b**). Together, the expression of
260 classical HLA immune machinery and checkpoint inhibitors by GSC-derived GBMO would, in theory, enable
261 direct interaction with T cells.
262
263 Next, we leveraged CIBERSORT[46], an *in-silico* cell-sorting tool, to determine cell-type immune gene expression
264 across GBMOsc (**Fig. Supplementary Fig. 7b**). GBMO showed similarities in shared immune gene expression, except
265 GBMO-120 that included a sizable proportion of B-cell/plasma cell-related genes, GBMO-640 of M1 macrophage
266 associated genes, and GBMO-30 of mast cell related genes that were different from NSCO, indicating that despite
267 some shared program, the intrinsic immune gene expression is heterogenous and the molecular profile may dictate
268 heterogenus cell-cell interactions with different immune cells. To obtain a more refined view of these immune genes,
269 we evaluated each GBMO compared to NSCO using a collated list of published immune-associated genes (IAGs) from
270 the Immunological Genome Project reference database[47] and separated these genes into functional clusters
271 representing interleukins/interferons, sensome, secretome, and immune-associated transcription factors (IATFs).
272 This clustering yielded insights into GBMOsc immune-like expression (**Fig. 4e**). For example, most of the upregulated
273 IAGs in GBMO-1201 belong to secretome and interferon/interleukin classes, suggesting it may persistently release
274 immune molecules into the TME, like *CCL2* a chemoattract associated with poor prognosis in GBM. GBMO-640 show
275 expression of *SEMA6D*, *HLA-H* and *ERAP*2, a protease that function by trimming antigenic epitopes for presentation
276 by major histocompatibility complex (MHC) class I molecules. GBMO-30 showed increased *IL6A*, *IL32*, *IL1A*, *ERAP2*,
277 *HLA-B*. Although, there is heterogeneity in immune gene expression, there are some common shared molecules
278 among GBMOsc. To confirm our results and exclude the possibility that our transcriptome data had been confounded
279 by the presence of a few contaminant immune cells, we stained each GBMOsc for immune cell markers such as T cell-
280 specific glycoproteins, CD4 and CD8, and monocyte marker CD68. Indeed, we confirmed their absence in GBMOsc

281 (**Supplementary Fig. 8a**), indicating that these immune-associated genes (IAGs) are intrinsically expressed by
282 GBMOsc cells.

283

284 We next sought to correlate our organoids findings in vivo GBM, we turned to two published single-cell RNA-
285 seq data from GBM *in vivo* and examined the expression of key immune genes that we found upregulated.
286 Importantly, the analysis of these genes showed that our GBMO-intrinsic program is observed in tumors *in vivo* and it
287 is not a product of a potential *in vitro* phenomena. We analyzed 25 representative genes of our immune-like genes in
288 these two GBM datasets and found strong in vivo GBM cells intrinsically express immune molecules as shown in our
289 GBMOsc[48], supporting our observation that GSC-derived GBMOsc recapitulate an immune intrinsic gene expression
290 profile. In vivo, we found GBM genes with immune function can be classified *in vivo* as a) expressed in tumor
291 compartment only (intrinsic) b) expressed in both tumor compartment and infiltrating immune cells; or c) only on
292 immune cells (canonical immune genes), not observed in our GBMOs**.** These data are consistent with the observation
293 that NSCs and GSC express neuroimmune genes as they interact with immune cells directly, and may modulate the
294 shape the immune contributions by secreting chemokines and cytokines to the TME[20,22,23 20,21] **(Supplementary Fig.**
295 **8b,c).** We correlated the expression of MHC-class I and interferon genes in GBMO and single cell GBM observing that
296 interferon genes like *STAT1, IRF1, TAP1, IFITM1, IRF3, IRF9* are equally conserved in GBM and our GBMO. To confirm
297 the functional significance of this gene program we examined the effects of IL17 and IFN-γ in the size of GSCs in vitro.
298 We found that IFN-γ but not IL17 decreased the numbers of GBMO-forming GSCs tumorspheres with a concomitant
299 reduction of transcription factor myeloid Elf-1 like factor (MEF), also known as *ELF4*, reduction of *MEF/ELF4* leads to
300 loss of stemness of GBM[49]. **(Supplementary Fig. 9a-c)**. Altogether, these findings provide functional support
301 suggesting that the intrinsic immune program not only can produce molecules able to modulate the TME but also
302 create intrinsic immune vulnerabilities for GBM having intrinsic circuits that can modulate critical genes for stemness
303 in GBM.

304

305

306 **SATB2$^+$ and HOPX$^+$ progenitor populations drive immune expression in GBM *in vivo***

307 Having found discrete niches and cell type marker expression in GBMO, we sought to determine
308 which cells were driving the strong expression of immune genes in (**Fig, 4a**). Given that outer radial glia
309 express STAT transcription factors and functional IFN receptors[50,51], we hypothesized this population, along
310 with SATB2$^+$ cells, which are preferentially born from HOPX$^+$ oRG during normal neurogenesis, may
311 contribute to the immune expression of GBMO. To address this, we first analyzed cells that highly expressed
312 SATB2, HOPX, or both together in the dataset and compared the expression of critical ISGs between SATB2$^+$,
313 HOPX$^+$, SATB2$^+$HOPX$^+$, and HOPX$^-$SATB2$^-$ cells (**Fig 5a).** Strikingly, we found elevated levels across several

314 immune genes, including *STAT1*, *IRF3, IRF9*, *IFITM3*, *HLA-A*, and *TAP1* among others (**Fig. 5b**). We repeated
315 this in a separate single-cell GBM dataset and found similar results (**Fig. 5c**). To unbiasedly examine gene
316 signatures of this cell population on a global scale, we performed differential expression between the groups
317 and focused on the most upregulated genes in these cell populations. Pathway enrichment analysis in both
318 datasets revealed these populations shared an enrichment for genes related to epithelial mesenchymal
319 transition, interferon gamma, and interferon alpha signaling (**Fig. 5d, e**). To gain insights to the active
320 immune-related networks of SATB2$^+$ and HOPX$^+$ cells, we then performed protein-protein interaction
321 analysis, focusing on the topmost upregulated interferon stimulated genes (**Fig. 5f, g**). While these two
322 populations shared some proteins like, *TAP1*, *XAF1,* and *CD74*, there were also some cell-type-specific
323 proteins, including *HLA-C* and *IFITM3* in HOPX$^+$ cells and *STAT1* and *STAT2* in SATB2$^+$ cells. To confirm these
324 findings from in vivo GBM to our GBMO at the protein shown at RNA level in (**Fig, 4a**), we performed
325 confocal analysis on the expression of IFN-γ receptors and STAT1 in SATB2$^+$ and HOPX$^+$ cells. Immunostaining
326 revealed that STAT1 and IFNGR1 were indeed expressed by these cells in GBMO-965 and -1201, indicating
327 that our GBMO recapitulate part of the immune gene landscape of HOPX$^+$ and SATB2$^+$ populations from GBM
328 *in vivo* (**Fig. 5h, i**).
329
330 **Discussion**
331
332 In this study, we performed a detailed characterization of the intrinsic properties of patient-derived
333 GBMO from GSCs to significantly expand our understanding of the remarkable ability of GSCs to form a 3D
334 tumor environment from a small, highly malignant group of stem cells (**Supplementary Fig 10**). We
335 demonstrated GSC-derived GBMO recapitulate histological, molecular, metabolic, genetic, and immune
336 features of GBM *in vivo*[52]. Our study importantly shows that GSCs have an encoded developmental memory
337 for 3D tumor evolution that endows them with the ability to give rise to GBMOsc *in vitro*. This is a
338 significant difference from past studies in which GBMO were generated from an established, heterogenous
339 pathological tissue that already has self-organization and a TME. By characterizing the intrinsic programs of
340 GBMO in the absence of immune and vascular contamination, we found an unexpected immune program
341 enriched in GSC-derived cell populations. Accordingly, our GSC-derived GBMO model provides a unique
342 platform to understand basic GBM biology and evolution.
343
344 In characterizing the spatial organization of GBMO, we discovered the *in vitro* recapitulation of oRG-like cells
345 in GBMO that have been recently identified in GBM in vivo[31]. These oRG-like GBM cells, distinguished by two oRG-
346 specific markers, p-VIM and HOPX, were present in all patient-derived GBMOsc, despite having distinct
347 transcriptomic profiles (**Fig. 2**), suggesting they may be a ubiquitous cell type in GBM, though more work is needed to
348 conclude this definitively. Underscoring their importance is the intriguing hypothesis which speculates that human
349 GBM initiation originates with aberrant reactivation of the oRG genetic program[50]. In our GBMOsc, these oRG-like
350 tumor cells showed migratory phenotypes and localized to the leading-edge during mitosis. It has also been

351 recognized that a subpopulation of oRG may contain an intrinsic mesenchymal population[53], perhaps explaining their
352 ability to express immune genes in GBM. Our GBMOsc also recapitulated the presence of SATB2$^+$ tumor cells that
353 drive GBM pathology. In normal human brain development, oRG preferentially differentiate into SATB2 upper-layer
354 neurons. Thus, it is tempting to speculate that SATB2 expression may simply be a gene activated downstream of the
355 aberrant deployment of an HOPX oRG-like program, rather than its own malignant progenitor. Indeed, we noted a
356 large portion of cells co-expressing these genes in both single cell RNA-seq datasets. Nevertheless, these novel
357 observations demonstrate that patient-derived GSCs have an encoded ability to give rise to highly malignant
358 progenitors and add to growing evidence that GBM growth and invasiveness may rely on malignant hijacking of the
359 oRG-like and SATB2 gene program. This work also highlights the utility of GBMO for studying GBM biology in a
360 dynamic, 3D cellular system. The insights gained from this level of complexity in recapitulating aspects of tumor
361 biology could not have been achieved by culturing GSCs as tumorspheres *in vitro* (**Supplementary Figure 10**).

362

363 There are several models of GBMO, each with different derivations and nomenclature, including 1)
364 genetic activation of oncogenes in normal organoids[4,12]; 2) invasion of normal iPSC-derived brain organoids
365 by GSCs[13,16]; 3) GBM organoids derived from fresh pieces of GBM, which include stromal vessels and
366 immune cells[14]; and 4) GSC-derived GBM organoids plus EGF/FGF[15] and our GBMO system. These models
367 have their own unique advantages and limitations for studying the contributions of the distinct cellular
368 compartments in GBM evolution. Although all GBMO models are limited by the absence of vasculature, we
369 suggest that GSC-derived models may be best suited to model the pre-vascular stages of GBM before initial
370 interactions between tumor, immune, and endothelial cells occur that determine the TME and lead to
371 explosive growth, angiogenesis, and invasion. Therefore, our results support the hypothesis that initial
372 GBM cells would harbor a heterogenous intrinsic immune program that influence, via cell-to cell and
373 paracrine interactions the formation of the TME long before massive vascularization, when major classical
374 immune infiltration happens and underscore that heterogeneity of TME may reside in the intrinsic immune
375 make up of the forming GBM stem and differentiated cells as shown in our GBMOs system.
376 We capitalized on this opportunity to determine novel tumor-autonomous mechanisms and found
377 strong expression of HLA, tapasin, and interferon genes in GBMO, which using single-cell RNA-seq data, we
378 localized to oRG-like HOPX$^+$ and SATB2$^+$ cells. We demonstrated the functional role of this pathway and
379 showed that IFN-γ, a cytokine produced by CD8$^+$ T cells can target GBMO, causing a downregulation of
380 molecular pathways involved in stemness. Our data support the hypothesis that GBM may have an intrinsic
381 vulnerability for CD8$^+$ T cells, including molecules like IFN-γ but this is negated by the powerful influence of
382 GBM cells secreting or harboring molecules like PDL1/2 that induce anergy in infiltrating immune cells. In
383 fact, our model is supported by recent data from a GBM clinical trial that suggest that reverting the T cell
384 exhaustion in GBM by anti-PD1 immunotherapy leads to a restoration of IFN-γ producing T cells and
385 improvement in survival benefit due to T cell targeting of the tumor via IFN-γ[54]. Whether such benefit
386 derives from preferential targeting of the highly invasive and immunogenic HOPX$^+$ and SATB2$^+$ cell

387 populations (**Fig. 6**) warrants future investigation. Our model should be useful to answer such questions,
388 model tumor specific immune inhibitors, and patient immune cells toward dissecting the immune circuitry
389 of the early TME in a preclinical manner.
390
391 Despite the insights into immune biology we found in our GSC-derived GBMO, future GBMO studies
392 will also benefit from incorporating interactions with stromal, vascular, and immune compartments. For
393 instance, the lack of vasculature can be overcome by implantation of organoids orthotopically in mice,
394 though future studies will need to clarify the translational relevance of a xenotransplanted model for
395 studying immune interactions versus co-culturing organoids with immune cells from the same patient[14].
396 Other future approaches for vascularization could implement microfluidics on a chip with human vascular
397 and immune cells to expand our pre-angiogenic model to a more in vivo-like model. Moreover, whether
398 differences exist in the biology of GBMO seeded from initial, naive GSCs, as modeled here, versus
399 recurrent, therapy resistant GSCs will be another important question to investigate.
400
401 In conclusion, we demonstrate GSC-derived GBMO can not only model the unique microanatomy of
402 early 3D tumor formation in the pre-angiogenic/immune stage, but also enable precise identification of
403 intrinsic molecular programs that drive early tumor growth and invasion. To this end, we found a unique
404 neuroimmune and progenitor phenotype that raises questions into the role of the intrinsic immune programs
405 expressed by these malignant progenitors at the earliest stages of TME and tumor evolution. Our GBMO
406 platform thus can serve as a model for future studies seeking to understand both basic GBM biology as well
407 as patient-specific intrinsic vulnerabilities of GSCs in the formation of a complex 3D tumor environment.
408 Much like creating a patient's tumor avatar, GSC-derived GBMO provide an opportunity for pre-clinical
409 interrogation of patient-derived cells toward personalized treatments for GBM, which currently has a median
410 survival of only 18 months[23].
411
412

413

414 ## Online Methods

415

416 **Generation of organoids and cell culture.**

417 Human GBM stem cells (GSCs) were procured from patients and allocated for human research purposes, per
418 the protocols approved by the Institutional Review Boards (IRB) at The Ohio State University Wexner Medical Center
419 and Mayo Clinic[24,25]. Confirmatory biological properties as GSCs for these lines has been demonstrated elsewhere
420 (**Table 1**). Patient-derived GSCs were isolated and cultured in Neurobasal, 2% B27 supplement without Vitamin A,
421 Glutamax, Antibiotic-Antimycotic (Thermo Fisher Scientific, Waltham, MA, USA), 50 ng/ml human epidermal growth
422 factor (EGF), 50 ng/ml basic fibroblast growth factor (FGF) (R&D Systems, Minneapolis, MN, USA), and heparin
423 (Millipore Sigma, Billerica, MA, USA) in low-attachment cell culture flasks, as previously described[14]. Human neural
424 stem cells (NSC, H9 hESC-Derived, Invitrogen) were cultured on Geltrex in KnockOut DMEM/F12, 2% StemPro Neural
425 supplement, Glutamax, Antibiotic-Antimycotic (Thermo Fisher Scientific), 50 ng/ml human EGF, 50 ng/ml human FGF in
426 low-attachment cell culture flasks, several subclones were generated for the study. For GBM and NSC organoid
427 formation, dissociated single cells were cultured with GBM or NSC growth media for 4-7 days. GBM or normal
428 neurospheres were transferred to Matrigel droplets (BD Bioscience, San Jose, CA, USA) by pipetting into cold Matrigel
429 on a sheet of Parafilm with 3 mm dimples. These droplets were allowed to gel at 37°C and were subsequently removed
430 from the Parafilm. After 4 days of stationary growth, the tissue droplets were transferred to a spinning bioreactor
431 containing organoid differentiation media including 48% Neurobasal, 48% DMEM/F12, 1% B27 supplement, 0.5% N2
432 supplement, 1% Glutamax, 0.5% MEM-NEAA, and 1% Antibiotic-Antimycotic[55]. Human iPSCs and iPSC-derived
433 organoids were generated as described previously[55]. All cell lines were handled in accordance with the IBC biosafety
434 practices and relevant ethical guidelines of The Ohio State University College of Medicine, Nationwide Children's
435 Hospital, and University of Connecticut Health that regulate the use of human cells for research.

436

437 **Histology and immunofluorescence.**

438 Tissues were fixed in 4% paraformaldehyde for 20 min at 4˚C followed by washing in PBS three times for 10 min.
439 Tissues were allowed to sink in 30% sucrose overnight, embedded in OCT compound (Tissue-Tek, Sakura Finetek USA,
440 Torrance, CA, USA), and then cryosectioned at 20 μm. Tissue sections were stained with hematoxylin and eosin, and
441 images were taken with a light microscope (BX41, Olympus, Tokyo, Japan) equipped with a digital camera (DP71,
442 Olympus). For immunofluorescence, sections were incubated successively with 0.25% Triton X-100 and 4% normal
443 horse serum in PBS for 30 min, primary antibodies overnight, and Alexa Fluor 488-, 594-, or 647-conjugated species-

444 specific secondary antibodies for 2 h (Thermo Fisher Scientific). Vectashield Mounting Medium with DAPI (Vector
445 Laboratories, Burlingame, CA, USA) or DAPI (Thermo Fisher Scientific) were used for counterstaining. For single
446 labeling of tissue, the following primary antibodies against the following molecules (immunized species) were used:
447 activated-caspase-3 (559565, BD Pharmingen, San Jose, CA, USA), AHR (ab190797 and ab2769, Abcam), BNIP3 (sc-
448 56167, Santa Cruz Biotechnology), CD4 (550278, BD Pharmingen), CD68 (556059, BD Pharmingen), CD8 (sc-18913,
449 Santa Cruz), CTIP2 (ab18465, Abcam), HOPX (HPA030180, Millipore Sigma), IFNGR1 (MABF753, MilliporeSigma), Ki-67
450 (ab16667, Abcam), PAX6 (AB_528427, DSHB, Iowa city, IA, USA), phosphorylated-vimentin (D076-3, MBL, Nagoya,
451 Japan), REELIN (MAB5366, Millipore Sigma), SATB2 (ab92446, Abcam), SOX2 (AF2018, R&D systems), STAT1 (610185,
452 BD Bioscience), TBR1 (ab31940, Abcam), TBR2 (ab23345, Abcam), and vimentin (sc7557, Santa Cruz). Images were
453 taken with a confocal laser-scanning microscope (LSM800, Carl Zeiss Microscopy GmbH, Jena, Germany).

454

455 **Quantitative analysis of immunostaining.**

456 Markers for proliferation and apoptosis (Ki-67 and activated-caspase-3) were quantified and normalized with
457 respect to nuclear DAPI staining, on the outer and inner surface areas of organoid images. Using ImageJ software,
458 quantification of marker staining was performed in 3 equally sized rectangular areas that were overlayed on each
459 outer and inner surface. A minimum of three sections were quantified for each organoid line. The length of relative
460 layer thickness was measured using ImageJ software.

461

462 **Targeted parallel sequencing and CNV analysis.**

463 A custom capture-based, targeted next-generation sequencing panel, which includes probes covering the
464 coding sequences of 407 cancer-related genes and genome-wide copy number variation (CNV) of backbone targets
465 (Agilent OneSeq 300kb CNV Backbone + custom panel), was utilized in this study. Sequencing libraries were produced
466 using standard methods, barcoded, and sequenced in pools on a HiSeq4000 by the OSU-CCC Solid Tumor
467 Translational Science Shared Resource. Experimental DNA samples were run side-by-side with a human reference
468 DNA sample. Raw sequence reads were aligned with bwa-0.7.13[56] aln and sample to Homo sapiens genome 1000g
469 v37. Alignment was converted to bam with samtools v1.3.1[57]. After adding read groups, marking duplicates, and
470 sorting with picard 2.4.1[58], Genome Analysis Toolkit (GATK) v3.6[59] was used to realign around indels. Mpileup format
471 was generated with samtools v1.3.1 requiring quality > 1 and varscan v2.4.1[60] ProcessSomatic and Variant Effect
472 Predictor from ensembl[61] were used to identify tumor-specific variants for each sample. Variants were filtered for
473 location (excluding non-coding variants), coding impact (excluding LOW impact variants – those unlikely to change

474 protein behavior), allele frequency in public databases (excluding common variants found in 1000g[62] and ExAC[63]), and
475 known variants (excluding variants listed in NCBI dbSNP[64] but not in COSMIC databases[65]). CNVkit, a python-
476 based copy number calling software[66], was used to detect the copy number alterations from the samples using
477 a single human "normal" sample as the reference. The log r ratios were calculated for both target and anti-target bins
478 across the genome. Segmentation was performed on the binned data using the circular binary segmentation
479 algorithm. For the heat maps, segments with medians greater than 0.25 were considered duplications and those with
480 medians less than -0.5 were considered deletions.

481

482 **Real-Time Quantitative PCR.**

483 RNAs were extracted from cell cultures with QIAzol reagent and miRNeasy Mini Kit (QIAGEN, GmbH, Hilden,
484 Germany), following the manufacturer's protocol. cDNAs were obtained from 500 ng of mRNA using the
485 retrotranscription kit (Thermo Fisher Scientific). Quantitative real-time PCR was performed on 1/20 of the
486 retrotranscription reaction using SYBR Green PCR Master Mix (Thermo Fisher Scientific). Primers were designed to
487 amplify 50- to 200-bp fragments; All primer sequences can be found in Table 2. The qPCR data were assessed using
488 delta-delta CT for evaluating results in the sigmoid region of the amplification curve. For each analysis, samples were
489 normalized by comparison with the housekeeping gene GAPDH. All samples, including "no template" controls, were
490 assayed in triplicate. Each experiment was performed three times with comparable results. Data are expressed as
491 mean ± SEM.

492

493 **Transcriptome analysis and differential expression.**

494 The GeneChip Human Transcriptome Array 1.0 (also known as Clariom D assays; Affymetrix, Thermo Fisher
495 Scientific Inc.) was used to provide a detailed analysis of the organoid transcriptome. Briefly, 100 ng of total RNA
496 from each of the three samples originally assigned for microarray analysis were used to generate amplified and
497 biotinylated sense-strand cDNA from the entire expressed genome according to the GeneChip WT PLUS Reagent Kit
498 User Manual (P/N 703174, Affymetrix Inc., Santa Clara, CA). cDNA was hybridized to GeneChip Human Transcriptome
499 Array 1.0 for 16 hr in a 45°C incubator, rotated at 60 rpm. After hybridization, the microarrays were washed, and
500 then stained using the Fluidics Station 450 followed by scanning with the Affymetrix GeneChip Scanner 3000 7G,
501 according to manufacturer's instructions. Raw intensity data was normalized using the quintile normalization of
502 robust multiarray average (RMA) method (performed at the individual probe level). Probes with low-variance were
503 filtered out using the R package genefilter[67] and annotated to the human genome using the Human Clariom D

504 platform. Transcripts were identified as differentially expressed using the limma package[68], with a threshold of FDR-
505 adjusted p-value <0.05 and fold change greater than ±2.

506

507 **Principal component and subtype analysis, hierarchal clustering, and functional annotation.**

508 We reduced the dimensionality of the data by performing principal component analysis (PCA) on the
509 organoid microarray datasets using the prcomp function in R (center = TRUE, scale = FALSE), including only the
510 filtered genes with moderate to high variance. The average relative expression of each set of GBM subtype predictor
511 genes (as defined by TCGA[36] was quantified from the log2-transformed expression values to determine a relative
512 subtype score for defining each GBMO line. Subtype average expression was normalized by the average log2
513 expression value of all subtype genes. To identify potential transcriptional modules based on the co-expression of
514 genes in the organoid dataset, unsupervised hierarchical clustering of differentially expressed genes (DEGs) was
515 performed using average linkage and uncentered Pearson correlation on variably expressed genes, as determined by
516 the varFilter() function in limma. Log2-scaled expression values were centered on the median before performing
517 hierarchical clustering. Heatmaps of clustered differential gene expression were then generated. Differentially
518 expressed gene data and the resulting clusters (FC±2, p<0.05) were exported for further functional analysis. We
519 made use of Enrichr, which utilizes the Fisher exact test with multiple hypothesis testing correction[69], to determine
520 gene ontologies, dysregulated pathways, and predicted upstream transcription factors.

521

522 **Unbiased search strategy for GSC molecular vulnerabilities.**

523 To establish an unbiased GBMO-intrinsic genetic program, normalized intensity values for each GBMO line
524 were first filtered to include only the top one-third of highly expressed genes. The resulting gene lists were compared
525 among GBMO lines and the genes shared by all four lines were the only ones further considered. Gene lists were
526 inputted into Enrichr for enrichment analyses and CIBERSORT[46] was utilized for *in silico* enumeration of interacting
527 immune cell subsets from GBMO transcriptomic data using default parameters. To further ascertain the immune
528 expression states of each GBMO line, we concentrated on the expression of immune-associated genes, as obtained
529 from ImmPort (http://www.immport.org/immport-open/public/home/home) and InnateDB
530 (http://www.innatedb.com)[70], using the original DE analyses to ensure all IAGs were encompassed. Plots were
531 produced using ggplot2 package in R. Again, the convergence of the DE IAGs was utilized and then filtered to focus
532 only on known human transcription factors, as specified by http://fiserlab.org/tf2dna_db//index.html. For heatmap

533 generation, data were imported into the online matrix software, Morpheus
534 (https://software.broadinstitute.org/morpheus).

535

536 **Processing of single-cell RNA-seq datasets from GBM *in vivo*.**

537 Raw read count matrices for Neftel et al[71] and Muller et al
538 (https://www.biorxiv.org/content/10.1101/377606v1.full[72]) were downloaded from GSE131928 and UCSC Single Cell
539 Browser (https://cells.ucsc.edu/), respectively. A Seurat object was created for each matrix separately and datasets
540 were scaled. The expression of *HOPX* and *SATB2* were then visualized. In each dataset, an expression cut-off of 50%
541 of maximal gene expression was established and all cells expressing at or above this were deemed to be $HOPX^+$ or
542 $SATB2^+$. Since we found expression of these genes were not mutually exclusive, we created a third category,
543 $HOPX^+SATB2^+$, for cells expressing both these genes. Cell populations were identified according to these population
544 criteria and the expression of well-known immune associated genes visualized. Upregulated genes in each cell
545 population were then determined for each population using the FindAllMarkers command of Seurat v3 [73]. From
546 these upregulated gene lists, pathway analysis was performed using Enrichr. After noting an enrichment of immune-
547 related genes across both datasets, we extracted interferon stimulated genes from the upregulated interferon
548 stimulated genes. We then made use of StringDB (https://string-db.org/) to generate protein-protein interaction
549 networks for the top-25 upregulated ISGs of each cell population and merged these networks from each dataset
550 together.

551

552

553 **Retrospective analysis of gene expression in human gliomas.**

554 Gene expression of neurodevelopmental progenitor markers and upregulated GBMO genes were determined
555 across primary patient gliomas and subtypes of GBM tumors, determined through analysis of the National Cancer
556 Institute Repository for Molecular Brain Neoplasia Data (http://betastasis.com/glioma/rembrandt/) and TCGA
557 (https://tcga-data.nci.nih.gov/publications/tcga), respectively. Gene expression localization in structures of primary
558 patient GBM was determined through analysis of Allen Institute of Ivy GAP (http://glioblastoma.alleninstitute.org/).
559 Expression data was downloaded and heatmaps were generated using the matrix visualization software, Morpheus.
560 Heatmaps of Pearson similarity matrices were also generated using Morpheus. Detailed information of heatmaps,
561 including gene names in retained order as in **Supplementary Fig. 7** can be found in **Supplementary Tables 10-14**.

562

563 **Metabolic analysis of GBMO with Seahorse technology.**

564 For Seahorse Analysis (XFe96, Agilent Technologies), organoids were first dissociated via dissociation reagent.
565 Dissociated cells were washed into warmed Seahorse XF DMEM medium supplemented with 10 mM glucose, 1 mM
566 pyruvate, and 2 mM glutamine and plated at a density of $1x10^5$ cells/well on a poly-L-lysine coated XFe96 Seahorse
567 cell culture microplate. Cells were simultaneously tested for oxygen consumption rate (OCR) and extracellular
568 acidification rate (ECAR) per the manufacturer's XF Real-Time ATP Rate Assay Kit protocol. Mitochondrial ATP
569 (mitoATP) and glycolytic ATP (glycoATP) production rates were calculated via Agilent Seahorse XF Real-Time ATP Rate
570 Assay Report Generator. ATP Production Rates were analyzed via t-test or ANOVA with Bonferroni posthoc
571 corrections as needed, with significance set at $p<0.05$.

572

573 **Statistical analysis.**

574 All data were included for statistical analyses using GraphPad Prism 6.0. Unpaired Student's t-test (two-
575 tailed) was used for the comparison between two unpaired groups and one-way ANOVA was applied for multi-group
576 data comparisons. The variance was similar between the groups that were being statistically compared. All data met
577 the assumptions of the tests. Survival estimates were calculated using the Kaplan–Meier analysis. Briefly, the
578 expression levels of target genes and patient survival information from the TCGA database were loaded into X-Tile as
579 a tab-delimited text file. By running 'Kaplan–Meier' program, the cohort was then divided into two data sets with the
580 optimal cut points generated according to the highest w2-value defined by log-rank test and Kaplan–Meier analyses.
581 Bar graphs were presented as means ± SEM. with statistical significance at $*P < 0.05$, $**P < 0.01$, or $***P < 0.001$.

582

583

584

585 **FIGURE AND FIGURE LEGENDS**

586

587 **Figure 1. Deep characterization of GBMO defines layering organization, patient-specific differences, and partial co-**
588 **optation of a developmental program.** (**a)** Approach for studying patient-derived glioblastoma in the GBM organoid
589 model. **(b)** Representative Immunohistochemistry for vimentin (VIM), proliferative (Ki-67), apoptotic (active-caspase-
590 3 (A-Cas)), and hypoxia (BNIP3) markers in GBMO-30 and induced pluripotent stem cell organoid (iPSCO). Scale bar,
591 50 µm. **(c-e)** Quantification of Ki-67-positive (c) and A-Cas-positive (d) cells, and relative thickness of proliferative and
592 apoptotic areas (e) in iPSCO and patient-derived GBMOs. Bar graphs are presented as means ± SEM. Two-tailed
593 unpaired Student's t-test. (Ki-67: GBMO-30, $P < 0.0001$; GBMO-965, $P = 0.0009$; GBMO-1201, $P = 0.0173$; iPSCO, $P =$
594 0.0008. A-Cas, GBMO-30, $P = 0.0001$; GBMO-965, $P = 0.0423$; GBMO-1201, $P = 0.0011$; iPSCO, $P = 0.0225$.) **(f)**
595 Immunofluorescent images for quiescent/stress marker ATF4 in GBMO-30, 965 and 1201. **(g)** Sample images of
596 immunostaining for VIM, and HOPX markers of outer radial glia in iPSCO, GBMO-30, -965, -1201, and neural stem cell
597 organoid (NSCO). Scale bar, 20 µm. **(h)** Immunostaining for the stem cell marker SOX2 and deep-layer neuron marker
598 CTIP2 in iPSCO, NSCO, and GBMO lines. Scale bar, 50 µm.

599

600 **Figure 2. Characterization of markers for progenitor diversity in GBMO and their expression in vivo. (a)**
601 Representative confocal images for immunostaining of Cajal-Retzius cell (top: REELIN), deep-layer cortical
602 neuron (top: TBR1, second: SATB2), intermediate progenitor (second: TBR2), and radial glia (second and
603 third: PAX6) markers in iPSCO, hNSO, and each GBMO line. Scale bar, 20 µm. **(b)** Violin plots of marker
604 mRNA expression by molecular subtype using publicly available TCGA cohorts. Cla, Classical; Mes,
605 Mesenchymal; Pro, Proneural; and Nor, Normal. One-way ANOVA followed by Dunnett's correction,
606 relative to Normal. (*CTIP2*: Cla, $P < 0.0001$; Mes, $P < 0.0001$; Pro, $P < 0.0001$. *PAX6*: Mes, $P < 0.01$. *REELIN*:
607 Cla, $P < 0.0001$; Mes, $P < 0.0001$; Pro, $P < 0.0001$. *SATB2*: Cla, $P < 0.0001$; Mes, $P < 0.0001$; Pro, $P < 0.0001$.
608 *SOX2*: Cla, $P < 0.0001$; Mes, $P < 0.0001$; Pro, $P < 0.0001$. *TBR1*: Cla, $P < 0.0001$; Mes, $P < 0.0001$; Pro, $P <$
609 0.0001. *TBR2*: Mes, $P < 0.01$. VIM: Cla, $P < 0.0001$; Mes, $P < 0.0001$; Pro, $P < 0.0001$.). N.S. = not significant,
610 $P > 0.05$. **(c)** Schematic of tissue-like organization and progenitor diversity in iPSCO and GBMO, color bands
611 represent the localization or absence of specific progenitor organized in layers in the normal organoids
612 compared to glioblastoma organoids.

613

614 **Figure 3. Mutational, transcriptomic and functional metabolic landscape of patient derived GBMO. (a)** Diagram of
615 genomic sequencing and microarray analysis for GSC-derived glioblastoma organoid intrinsic molecular phenotypes.
616 **(b)** Large-scale copy number variant (CNV) analysis of GBMO-1201, -640, -965, -30, and NSCO (-01, -02 are technical
617 replicates from different batches). Red, amplifications; blue, deletions. **(c)** Mutational classification in GBMO lines
618 and NSCO, as defined by Catalogue of Somatic Mutations in Cancer (COSMIC). **(d)** Summary of somatic mutation
619 types and functional classification of mutated genes in each GBMO line and NSCO. Complete details are found in
620 **Supplemental Table 3**. **(e)** Quantification of mutation types indicates an enrichment of damaging, coding mutations
621 in GBMO-30, -965, -1201, -640, relative to NSCO. Indel, insertion and/or deletion. **(f)** Transition/transversion (Ti/Tv)
622 proportion comprising single-nucleotide variants for GBMO-30, -965, -1201, -640, and NSCOs, as identified by TPDS.
623 **(g)** Principal component analysis (PCA) of GBMO and NSCO transcriptomes. **(h)** Relative expression of classifier genes
624 belonging to each GBM molecular subtype **(i)** Metabolomic profiles, as inferred from transcriptomic analysis, of each
625 GBMO line and adjoining summary schematic of classical biochemical pathways. 1,3-BPG, 1,3 Bisphosphoglycerate; F-
626 1,6-BP, Fructose-1-6-Bisphosphate G-6-P, Glucose-6-Phosphate; PPP, Pentose Phosphate Pathway; TCA, Tricarboxylic
627 Acid. **(j)** Expression and schematic of genes involved in the methionine cycle in GBMO and NSCO. GBMO-30, GBMO-
628 965, and GBMO-1201). **(k)** Metabolic analysis with Seahorse XF Real-Time ATP Rate Assay of GBMO-30, 965, 1201
629 and hNSCO showing mitochondrial ATP (Mito ATP) and glycolytic ATP (Glyco ATP) production rates. Total ATP
630 production: $p<0.0001$, mito ATP: $p<0.0001$, glycol ATP: $p<0.0001$. **(l)** Oxygen Consumption Rate (OCR) and **(m)**
631 Extracellular Acidification Rate (ECAR) were measured among hNSCO and each GBMO.

632

633

634 **Figure 4. GBMO intrinsic program analysis reveals enrichment of immune genes. (a)** Hierarchical clustering
635 heatmap of differential gene expression between all GBMO and NSCO with gene ontology for each of the five
636 identified gene clusters. Selected genes from each cluster are highlighted on the right. **(b)** Heatmap for
637 transmembrane proteins of immune system (CDs, PDs, and HLAs) in each GBMO and hNSCO. **(c)** Schematic workflow
638 for identifying genes comprising the GBMO intrinsic program. Briefly, we focused on the shared top 33% of expressed
639 genes from each GBMO line. **(d)** Gene ontology (*right*) enrichment analysis of GBMO intrinsic program genes. **(e)**
640 Volcano plots of differential expression of immune genes for each GBMO line, relative to NSCO. Genes are colored by
641 immune category if differentially expressed (logFC > ±2, adj. *p*-value < 0.05).

642

643

644 **Figure 5. HOPX$^+$ and SATB2$^+$ cell populations drive immune expression in GBM. (a)** UMAP plot for *in vivo* GBM
645 single-cell RNA-seq data from Neftel et al[71]. Individual cells are colored according to their high expression (greater
646 than 50% maximum value) of SATB2 (pink), HOPX (orange), both SATB2 and HOPX (blue), or neither (grey). **(b)** Violin
647 plots for representative immune associated genes for each cell population from Neftel et al. **(c)** Violin plots for
648 representative immune associated genes for each cell population from an independent dataset, Muller et al, in which
649 resected GBM were processed for single-cell RNA-seq using 10X Genomics. **(d, e)** Pathway enrichment analysis for
650 genes upregulated in SATB2$^+$, HOPX$^+$, SATB2$^+$HOPX$^+$ cells in Neftel et al (d) or Muller et al (e)**.** Grey line denotes 5%
651 level of significance threshold for log-adjusted P-value scores. **(f, g)** Protein-protein interaction network of
652 upregulated interferon stimulated genes in SATB2$^+$ and HOPX$^+$ cells. Nodes are colored by which dataset they were
653 found to be upregulated. Green, Muller et al; Yellow, Neftel et al. **(h)**. Confirmation of expression of interferon
654 related genes on SATB2 and HOPX cancer progenitors. Representative confocal images for immunostaining of STAT1,
655 IFNGR in HOPX and SATB2 populations in 3D reconstruction and z-stacking in GBMO 1201 and 965. Scale bar, 20 µm

656

657

658 **Figure 6. GBM organoid model and novel intrinsic phenotypes**. 3D model of a GSC-GBMO organoid summarizing
659 our novel findings, including SATB2 and HOPX oRG-like progenitors that are characterized as bona-fide glioma stem
660 cells. diverse microanatomical domains and hypoxic microenvironments, intrinsic immune program enriched with
661 MHC-class I, interferon and inhibitory pathways in SATB2 and HOPX oRG cells.

662

663

664

665 **EXTENDED DATA**

666

667 **Supplementary Figure 1. Selected Patient MRI and histopathology of parental tumors**
668 **and corresponding GBMO (Related to Figures 1 and 2). (a, b)** Coronal and sagittal MRI slices and tissue pathology of
669 brain tumor patients #965 (left) and #1201 (right). **(c)** Experimental procedure from resected brain tumor to GBM
670 organoids via glioblastoma stem cells (GSCs). **(d, e)** Histological analysis by hematoxylin and eosin (H&E) staining
671 using parental tumor tissue and patient-derived GBM organoid 965 (GBMO-965, left) and 1201(GBMO-1201, right).
672 Red arrows, elongated cells; Orange arrows, syncytia; Blue arrows, fibrils; Green arrows, fusiform cell clusters; Yellow

673 arrows, cells with clear cytoplasm; Black arrows, highly chromatic nuclei. Scale bars, 100 µm. **(f)** Success rate for
674 generating GBMO in different patient derived-glioblastoma stem cells, a total of 226 organoids were generated.

675

676 **Supplementary Figure 2. Comparison of in vitro modeling of GBM biology between GBMO and GSC tumorspheres**
677 **(Related to Figures 1 and 2). (a)** Comparison of features between GBM tumorsphere and GBM organoid (GBMO). **(b)**
678 Immunocytochemistry for Ki-67, active-caspase-3 (A-Cas), HIF-1α, and vimentin with GBM-30 GSCs on poly-lysine (2D
679 culture). Bar graphs are presented as mean ± SEM. Two-tailed unpaired Student's *t*-test (N.S. = not significant, $P >$
680 0.05).

681 **Supplementary Figure 3. Additional characterization of proliferation, apoptosis, and hypoxia in additional**
682 **GBMO and hNSCO (Related to Figure 1).** (**a**) Representative images of vimentin (VIM) immunostaining in
683 patient-derived organoid from GBM 30, 965, 1201 and 640 (GBMO-30, GBMO-965, GBMO-1201, and
684 GBMO-640) and an organoid derived from human neural stem cells (hNSCO) and human induced
685 pluripotent stem cells (iPSCO). Scale bar, 20 µm. (**b**) Immunohistochemistry for proliferative (Ki-67) and
686 apoptotic (A-Cas) markers in GBMO-965, GBM-1201, GBMO-640, and hNSCO. Scale bar, 50 µm. **(c)**
687 Immunohistochemistry for hypoxia marker (BNIP3) in GBMO-965, GBM-1201, GBMO-640, and hNSCO.
688 Scale bar, 50 µm. **(d)** Negative control (no primary antibody) for each GBMO and iPSCO. **(e)** Hypoxia level
689 (BNIP3 intensity) from surface to inside in GBM-30, -965, -1201, and -640. **(f)** Quantitative analysis for
690 BNIP3 marker intensity between surface (0-150 µm) and inside (>150 µm from surface). **(g)** Sample images
691 of immunostaining for VIM and p-VIM : markers of outer radial glia in iPSCO, GBMO-30, -965, -1201, and
692 neural stem cell organoid (NSCO). Dotted lines highlight cleavage furrow of dividing cells. Scale bar, 20 µm.

693 **Supplementary Figure 4. Transcriptomic enrichment for immunity and cancer-related genes in GBMO**
694 **with confirmatory qPCR in GBMO and NSCO (Related to Figure 2). (a)** Pathway enrichment using
695 differentially expressed genes from GBMO (left) and NSCO (right). **(b)** Waterfall plot showing expression of
696 notable genes between GBMO-30, -965, -1201, and -640 and NSCO, as detected by transcriptomic analysis.
697 **(c)** Confirmatory qPCR indicates relative expression of differentiation marker genes (top) and cancer-
698 related genes (bottom) between GBMO and NSCO by qPCR. Data are presented as means ± SEM. Two-
699 tailed unpaired Student's t-test. (*NEUROD1*, $P = 0.0231$; *OLIG2*, $P = 0.0015$; *PAX6*, $P = 0.0002$; *SOX2*, $P =$
700 0.0015; *SOX9*, $P < 0.0001$; *ZIC1*, $P < 0.0001$; *EGFR*, $P = 0.0375$; *MEF*, $P < 0.0001$; *MYC*, $P < 0.0001$; *NF1*, $P <$
701 0.0001; *POU3F2*, $P < 0.0001$; *PPAT1*, $P = 0.0336$; *PRPS1*, $P = 0.0073$; *RCOR2*, $P < 0.0001$; *SALL2*, $P < 0.0001$;
702 *TP53*, $P = 0.0101$.). N.S. = not significant, $P > 0.05$.

703 **Supplementary Figure 5. In vivo expression of GBMO-upregulated genes in primary gliomas and GBM**
704 **subtypes (Related to Figure 2). (a)** Heatmap of upregulated genes between each GBMO line and NSCO.
705 Dotted boxes denote top twelve genes for each GBMO line. **(b)** Violin plots of upregulated GBMO genes in
706 vitro by glioma subtype in vivo, using publicly available TCGA expression data. Genes colored by which
707 GBMO line they are upregulated in. GBM, Glioblastoma; Astro, Astrocytoma; Oligo, Oligodendroglioma;
708 Nor, Normal. One-way ANOVA followed by Tukey's test, relative to Normal. (*ADAMTS9*: GBM, $P < 0.0001$;
709 Astro, $P < 0.05$; Olig, $P < 0.05$. *ANGPT2*: GBM, $P < 0.0001$. *BST2*: GBM, $P < 0.0001$. *CASP4*: GBM, $P < 0.0001$.
710 *CFI*: GBM, $P < 0.0001$. *CHI3L1*: GBM, $P < 0.0001$. *CLEC2B*: GBM, $P < 0.01$. *EFEMP1*: GBM, $P < 0.0001$; Astro, P
711 < 0.01. *EYA4*: GBM, $P < 0.01$. *IGFBP7*: GBM, $P < 0.0001$; Astro, $P < 0.0001$; Oligo, $P < 0.0001$. *IL1B*: Oligo, $P <$
712 0.05. *KCNE4*: GBM, $P < 0.001$. *MCOLN3*: GBM, $P < 0.001$. *PDGFRA:* Astro, $P < 0.01$; Oligo, $P < 0.001$. *PR2X7*:
713 Astro, $P < 0.01$; Oligo, $P < 0.001$. *RGS10*: Astro, $P < 0.01$. *SAMD9L:* Astro, $P < 0.001$. *SRPX*: GBM, $P < 0.0001$;
714 Astro, $P < 0.01$; Oligo, $P < 0.001$. *STEAP2*: GBM, $P < 0.0001$; Astro, $P < 0.0001$; Olig, $P < 0.0001$. *STK32A*:
715 GBM, $P < 0.01$; Astro, $P < 0.001$; Oligo, $P < 0.001$. *TMEM154*: GBM, $P < 0.0001$. *VSNL1*: GBM, $P < 0.0001$;
716 Astro, $P < 0.0001$; Oligo, $P < 0.0001$.) **(c)** Violin plots of upregulated GBMO genes by GBM molecular
717 subtype, using publicly available REMBRANDT cohorts. Genes colored by which GBMO line they are
718 upregulated in. Cla, Classical; Mes, Mesenchymal; Pro, Proneural; and Nor, Normal. One-way ANOVA
719 followed by Tukey's test, relative to Normal. (*ADAMTS9*: Cla, $P < 0.0001$; Mes, $P < 0.01$. *ANGPT2*: Pro, $P <$
720 0.01. *BST2*: Cla, $P < 0.001$; Mes, $P < 0.001$. *CASP4*: Mes, $P < 0.0001$. *CFI*: Cla, $P < 0.05$; Mes, $P < 0.0001$.
721 *CHI3L1*: Cla, $P < 0.0001$; Mes, $P < 0.0001$. *CLEC2B*: Mes, $P < 0.0001$. *EFEMP1*: Cla, $P < 0.001$; Mes, $P < 0.0001$.
722 *EYA4*: Cla, $P < 0.05$. *GATM*: Cla, $P < 0.001$. *IGFBP7*: Cla, $P < 0.0001$; Mes, $P < 0.0001$; Pro, $P < 0.01$. *IL1B*: Cla,
723 $P < 0.001$; Mes, $P < 0.01$; Pro, $P < 0.001$. *IL6*: Mes, $P < 0.001$; Pro, $P < 0.01$. *KCNE4*: Cla, $P < 0.01$; Mes, $P <$
724 0.001. *MGP*: Mes, $P < 0.001$. *P2RX7*: Cla, $P < 0.01$. *PDGFRA*: Pro,$P < 0.0001$. *POSTN*: Cla, $P < 0.001$; Mes, $P <$
725 0.0001. *PRRX1*: Cla, $P < 0.001$; Mes, $P < 0.0001$; Pro, $P < 0.01$. *SRPX*: Cla, $P < 0.001$; Mes, $P < 0.05$. *STEAP2*:
726 Cla, $P < 0.0001$; Mes, $P < 0.0001$; Pro, $P < 0.0001$. *STK32A*: Cla, $P < 0.05$; Mes, $P < 0.05$; Pro, $P < 0.01$. *VRK2*:
727 Pro, $P < 0.01$. *VSNL1*: Cla, $P < 0.0001$; Mes, $P < 0.0001$; Pro, $P < 0.0001$).

728 **Supplementary Figure 6. Spatially-resolved heatmap of GBMO-upregulated gene expression in GBM**
729 **microstructures in vivo (Related to Figure 3). (a)** Heatmap depicting the spatial expression of upregulated genes in
730 GBMO-30, -965, -1201, and -640 by tumor microanatomy. Complete details of gene names can be found in
731 Supplementary Table 3. RNA-Seq data of tumor structures is derived from IvyGAP. **(b)** Summary figure for these
732 heatmaps. The colors were matched in the circle with the structure colors from the heatmap. Dark colors mean high
733 expression; light colors mean less expression.

734 **Supplementary Figure 7. Enrichment of immune genes by GBMO intrinsic program analysis. (a)** Pathway
735 (*left*) enrichment analysis of GBMO intrinsic program genes. **(b)** *In silico* immune cell transcriptomic analysis
736 for each GBMO line using CIBERSORT to infer immune cell expression signatures within each GBMO line
737 and NSCO.

738

739 **Supplementary Figure 8. Gene expression for immune system molecules from GBM single-cell RNA-seq and**
740 **immunostaining for immune cell markers GBMO-30, GBMO-965, and GBMO-1201 and resected GBM tissue**
741 **(Related to Figures 5). (a)** Representative confocal images for immunostaining of CD4 (top), CD8 (middle), and CD68
742 (bottom) in each GBMO line and primary human GBM (positive control). Scale bar, 50 µm. **(b)** Expression of
743 immune-like molecules in the glioma cell vs. infiltrating T cells or macrophages. **(c)** Gene expression in a GBM single-
744 cell RNA-seq for molecules of immune system in vivo GBM.

745

746 **Supplementary Figure 9. Effects of cytokine in GBMO-forming GSCs self-renewal and *MEF/ELF4* gene expression.**
747 **(a)** Neurosphere formation of GBM-30 with IL-17 and IFN-γ. **(b)** Quantification of neurospheres number among IL-17
748 and IFN-γ -treated GBM-30 GSCs. **(c)** Gene expression of *MEF/ELF4* in GBM-30 with IL-17 and IFN-γ.

749

750 **Supplementary Figure 10. GSC-derived GBMO model and novel intrinsic phenotypes.** GSC-GBM organoid model
751 depicting observed novel phenotypes and microanatomy of GBMOs resembling GBMs in vivo.

752

753 **Acknowledgments**

754

755 We kindly thank Sarah Warner for technical expertise in microarrays, Drs. Erica Bell, Jessica Fleming, and Arnab
756 Chakravarti for guidance and design of the targeted next-generation sequencing panel, and The Ohio State
757 Comprehensive Cancer Center Solid Tumor Translational Science Core (Drs. Cynthia Timmers and Tom Liu) and
758 Biostatistics Core (Dr. Amy Webb and Asha Jacob Jannu) for their technical assistance. To Drs. Timothy P. Cripe MD,
759 PhD, and Sofia B. Lizarraga, PhD for their critical reading of the manuscript. The work was supported in part by the
760 NCI (CA016058) and P30 CA016058. AQH is supported by the NIH (CA200399, CA183827, CA195503, CA216855,

761 NS070024), as well as the Mayo Clinician Investigator Award and the State of Florida. VP is supported by grant K24CA
762 160777. JI was supported by the NRI research Award and The Biogen-UConn Collaboration grant.

763

764

765

References

1. Guerrero-Cazares, H., Attenello, F.J., Noiman, L. & Quinones-Hinojosa, A. Stem cells in gliomas. *Handb Clin Neurol* **104**, 63-73 (2012).

2. Guerrero-Cazares, H., Chaichana, K.L. & Quinones-Hinojosa, A. Neurosphere culture and human organotypic model to evaluate brain tumor stem cells. *Methods Mol Biol* **568**, 73-83 (2009).

3. Sachs, N. *et al.* A Living Biobank of Breast Cancer Organoids Captures Disease Heterogeneity. *Cell* **172**, 373-386 e10 (2018).

4. Bian, S. *et al.* Genetically engineered cerebral organoids model brain tumor formation. *Nat Methods* **15**, 631-639 (2018).

5. Dietrich, J., Imitola, J. & Kesari, S. Mechanisms of Disease: the role of stem cells in the biology and treatment of gliomas. *Nat Clin Pract Oncol* **5**, 393-404 (2008).

6. Lee, J.H. *et al.* Human glioblastoma arises from subventricular zone cells with low-level driver mutations. *Nature* **560**, 243-247 (2018).

7. Lathia, J.D., Mack, S.C., Mulkearns-Hubert, E.E., Valentim, C.L. & Rich, J.N. Cancer stem cells in glioblastoma. *Genes Dev* **29**, 1203-17 (2015).

8. Bezzi, M. *et al.* Diverse genetic-driven immune landscapes dictate tumor progression through distinct mechanisms. *Nat Med* (2018).

9. Wang, Q. *et al.* Tumor Evolution of Glioma-Intrinsic Gene Expression Subtypes Associates with Immunological Changes in the Microenvironment. *Cancer Cell* **32**, 42-56 e6 (2017).

10. Azari, H. *et al.* Isolation and expansion of human glioblastoma multiforme tumor cells using the neurosphere assay. *J Vis Exp*, e3633 (2011).

11. Ben-David, U. *et al.* Patient-derived xenografts undergo mouse-specific tumor evolution. *Nat Genet* **49**, 1567-1575 (2017).

12. Ogawa, J., Pao, G.M., Shokhirev, M.N. & Verma, I.M. Glioblastoma Model Using Human Cerebral Organoids. *Cell Rep* **23**, 1220-1229 (2018).

13. Linkous, A. *et al.* Modeling Patient-Derived Glioblastoma with Cerebral Organoids. *Cell Rep* **26**, 3203-3211 e5 (2019).

14. Jacob, F. *et al.* A Patient-Derived Glioblastoma Organoid Model and Biobank Recapitulates Inter- and Intra-tumoral Heterogeneity. *Cell* **180**, 188-204 e22 (2020).

15. Hubert, C.G. *et al.* A Three-Dimensional Organoid Culture System Derived from Human Glioblastomas Recapitulates the Hypoxic Gradients and Cancer Stem Cell Heterogeneity of Tumors Found In Vivo. *Cancer Res* **76**, 2465-77 (2016).

16. Goranci-Buzhala, G. *et al.* Rapid and Efficient Invasion Assay of Glioblastoma in Human Brain Organoids. *Cell Rep* **31**, 107738 (2020).

17. Imitola, J. Regenerative neuroimmunology: The impact of immune and neural stem cell interactions for translation in neurodegeneration and repair. *J Neuroimmunol* **331**, 1-3 (2019).

18. Zhu, C. *et al.* The Tim-3 ligand galectin-9 negatively regulates T helper type 1 immunity. *Nat Immunol* **6**, 1245-52 (2005).

19. Watanabe, F. *et al.* Generation of Neurosphere-Derived Organoid-Like-Aggregates (NEDAS) from Neural Stem Cells. *Curr Protoc* **1**, e15 (2021).

20. Imitola, J. *et al.* Neural stem/progenitor cells express costimulatory molecules that are differentially regulated by inflammatory and apoptotic stimuli. *Am J Pathol* **164**, 1615-25 (2004).

21. Imitola, J. *et al.* Directed migration of neural stem cells to sites of CNS injury by the stromal cell-derived factor 1alpha/CXC chemokine receptor 4 pathway. *Proc Natl Acad Sci U S A* **101**, 18117-22 (2004).

22. Merzaban, J.S. *et al.* Cell surface glycan engineering of neural stem cells augments neurotropism and improves recovery in a murine model of multiple sclerosis. *Glycobiology* **25**, 1392-409 (2015).

23. Al-Kharboosh, R. *et al.* Inflammatory Mediators in Glioma Microenvironment Play a Dual Role in Gliomagenesis and Mesenchymal Stem Cell Homing: Implication for Cellular Therapy. *Mayo Clin Proc Innov Qual Outcomes* **4**, 443-459 (2020).

24. Banasavadi-Siddegowda, Y.K. *et al.* PRMT5-PTEN molecular pathway regulates senescence and self-renewal of primary glioblastoma neurosphere cells. *Oncogene* **36**, 263-274 (2017).

25. Banasavadi-Siddegowda, Y.K. *et al.* PRMT5 as a druggable target for glioblastoma therapy. *Neuro Oncol* (2017).

26. Chaichana, K.L. *et al.* Preservation of glial cytoarchitecture from ex vivo human tumor and non-tumor cerebral cortical explants: A human model to study neurological diseases. *J Neurosci Methods* **164**, 261-70 (2007).

27. Qian, X. *et al.* Brain-Region-Specific Organoids Using Mini-bioreactors for Modeling ZIKV Exposure. *Cell* **165**, 1238-1254 (2016).

28. Fair, S.R. *et al.* Electrophysiological Maturation of Cerebral Organoids Correlates with Dynamic Morphological and Cellular Development. *Stem Cell Reports* **15**, 855-868 (2020).

29. Morrow, C.S. *et al.* Vimentin Coordinates Protein Turnover at the Aggresome during Neural Stem Cell Quiescence Exit. *Cell Stem Cell* **26**, 558-568 e9 (2020).

30. Singh, A. *et al.* The BH3 only Bcl-2 family member BNIP3 regulates cellular proliferation. *PLoS One* **13**, e0204792 (2018).

31. Bhaduri, A. *et al.* Outer Radial Glia-like Cancer Stem Cells Contribute to Heterogeneity of Glioblastoma. *Cell Stem Cell* **26**, 48-63 e6 (2020).

32. Wang, R. *et al.* Adult Human Glioblastomas Harbor Radial Glia-like Cells. *Stem Cell Reports* **14**, 338-350 (2020).

33. Suva, M.L., Riggi, N. & Bernstein, B.E. Epigenetic reprogramming in cancer. *Science* **339**, 1567-70 (2013).

34. Jaime-Ramirez, A.C. *et al.* Humanized chondroitinase ABC sensitizes glioblastoma cells to temozolomide. *J Gene Med* **19**(2017).

35. Tao, W. *et al.* SATB2 drives glioblastoma growth by recruiting CBP to promote FOXM1 expression in glioma stem cells. *EMBO Mol Med* **12**, e12291 (2020).

36. Cancer Genome Atlas Research, N. Comprehensive genomic characterization defines human glioblastoma genes and core pathways. *Nature* **455**, 1061-8 (2008).

37. Araujo, L.H. *et al.* Genomic Characterization of Non-Small-Cell Lung Cancer in African Americans by Targeted Massively Parallel Sequencing. *J Clin Oncol* **33**, 1966-73 (2015).

38. Forbes, S.A. *et al.* COSMIC: High-Resolution Cancer Genetics Using the Catalogue of Somatic Mutations in Cancer. *Curr Protoc Hum Genet* **91**, 10 11 1-10 11 37 (2016).

39. Kandoth, C. *et al.* Mutational landscape and significance across 12 major cancer types. *Nature* **502**, 333-339 (2013).

40. Liau, B.B. *et al.* Adaptive Chromatin Remodeling Drives Glioblastoma Stem Cell Plasticity and Drug Tolerance. *Cell Stem Cell* **20**, 233-246 e7 (2017).

41. Koschmann, C. *et al.* ATRX loss promotes tumor growth and impairs nonhomologous end joining DNA repair in glioma. *Sci Transl Med* **8**, 328ra28 (2016).

42. Verhaak, R.G. *et al.* Integrated genomic analysis identifies clinically relevant subtypes of glioblastoma characterized by abnormalities in PDGFRA, IDH1, EGFR, and NF1. *Cancer Cell* **17**, 98-110 (2010).

43. Wang, Z. *et al.* Methionine is a metabolic dependency of tumor-initiating cells. *Nature Medicine* **25**, 825-837 (2019).

44. Hanahan, D. & Coussens, L.M. Accessories to the crime: functions of cells recruited to the tumor microenvironment. *Cancer Cell* **21**, 309-22 (2012).

45. Nakasone, E.S. *et al.* Imaging tumor-stroma interactions during chemotherapy reveals contributions of the microenvironment to resistance. *Cancer Cell* **21**, 488-503 (2012).

46. Newman, A.M. *et al.* Robust enumeration of cell subsets from tissue expression profiles. *Nat Methods* **12**, 453-7 (2015).

47. Heng, T.S., Painter, M.W. & Immunological Genome Project, C. The Immunological Genome Project: networks of gene expression in immune cells. *Nat Immunol* **9**, 1091-4 (2008).

48. Wang, Q. *et al.* Tumor Evolution of Glioma-Intrinsic Gene Expression Subtypes Associates with Immunological Changes in the Microenvironment. *Cancer Cell* **33**, 152 (2018).

49. Bazzoli, E. *et al.* MEF promotes stemness in the pathogenesis of gliomas. *Cell Stem Cell* **11**, 836-44 (2012).

50. Pollen, A.A. *et al.* Molecular Identity of Human Outer Radial Glia during Cortical Development. *Cell* **163**, 55-67 (2015).

51. Pollen, A.A. *et al.* Establishing Cerebral Organoids as Models of Human-Specific Brain Evolution. *Cell* **176**, 743-756 e17 (2019).

52. Hambardzumyan, D. & Bergers, G. Glioblastoma: Defining Tumor Niches. *Trends Cancer* **1**, 252-265 (2015).

53. Eze, U.C., Bhaduri, A., Haeussler, M., Nowakowski, T.J. & Kriegstein, A.R. Single-cell atlas of early human brain development highlights heterogeneity of human neuroepithelial cells and early radial glia. *Nat Neurosci* (2021).

54. Cloughesy, T.F. *et al.* Neoadjuvant anti-PD-1 immunotherapy promotes a survival benefit with intratumoral and systemic immune responses in recurrent glioblastoma. *Nat Med* **25**, 477-486 (2019).

55. Lancaster, M.A. & Knoblich, J.A. Generation of cerebral organoids from human pluripotent stem cells. *Nat Protoc* **9**, 2329-40 (2014).

56. Li, H. & Durbin, R. Fast and accurate short read alignment with Burrows-Wheeler transform. *Bioinformatics* **25**, 1754-60 (2009).

57. Li, H. *et al.* The Sequence Alignment/Map format and SAMtools. *Bioinformatics* **25**, 2078-9 (2009).

58. Picard. Picard - A set of tools (in Java) for working with next generation sequencing data in the BAM format. http://broadinstitute.github.io/picard. *http://broadinstitute.github.io/picard*.

59. McKenna, A. *et al.* The Genome Analysis Toolkit: a MapReduce framework for analyzing next-generation DNA sequencing data. *Genome Res* **20**, 1297-303 (2010).

60. Koboldt, D.C. *et al.* VarScan 2: somatic mutation and copy number alteration discovery in cancer by exome sequencing. *Genome Res* **22**, 568-76 (2012).

61. McLaren, W. *et al.* The Ensembl Variant Effect Predictor. *Genome Biol* **17**, 122 (2016).

62. Genomes Project, C. *et al.* A global reference for human genetic variation. *Nature* **526**, 68-74 (2015).

63. Lek, M. *et al.* Analysis of protein-coding genetic variation in 60,706 humans. *Nature* **536**, 285-91 (2016).

64. Sherry, S.T. *et al.* dbSNP: the NCBI database of genetic variation. *Nucleic Acids Res* **29**, 308-11 (2001).

65. Bamford, S. *et al.* The COSMIC (Catalogue of Somatic Mutations in Cancer) database and website. *Br J Cancer* **91**, 355-8 (2004).

66. Talevich, E., Shain, A.H., Botton, T. & Bastian, B.C. CNVkit: Genome-Wide Copy Number Detection and Visualization from Targeted DNA Sequencing. *PLoS Comput Biol* **12**, e1004873 (2016).

67. Huber, W. *et al.* Orchestrating high-throughput genomic analysis with Bioconductor. *Nat Methods* **12**, 115-21 (2015).

68. Ritchie, M.E. *et al.* limma powers differential expression analyses for RNA-sequencing and microarray studies. *Nucleic Acids Res* **43**, e47 (2015).

69. Chen, E.Y. *et al.* Enrichr: interactive and collaborative HTML5 gene list enrichment analysis tool. *BMC Bioinformatics* **14**, 128 (2013).

70. Breuer, K. *et al.* InnateDB: systems biology of innate immunity and beyond--recent updates and continuing curation. *Nucleic Acids Res* **41**, D1228-33 (2013).

71. Neftel, C. *et al.* An Integrative Model of Cellular States, Plasticity, and Genetics for Glioblastoma. *Cell* **178**, 835-849 e21 (2019).

72. Muller, S.M., Elizabeth Di Lullo, Aparna Bhaduri, Beatriz Alvarado, Garima Yagnik, Gary Kohanbash, Manish Aghi, Aaron Diaz. A single-cell atlas of human glioblastoma reveals a single axis of phenotype in tumor-propagating cells. *https://www.biorxiv.org/content/10.1101/377606v1.full)* (2021).

73. Stuart, T. *et al.* Comprehensive Integration of Single-Cell Data. *Cell* **177**, 1888-1902 e21 (2019).

1

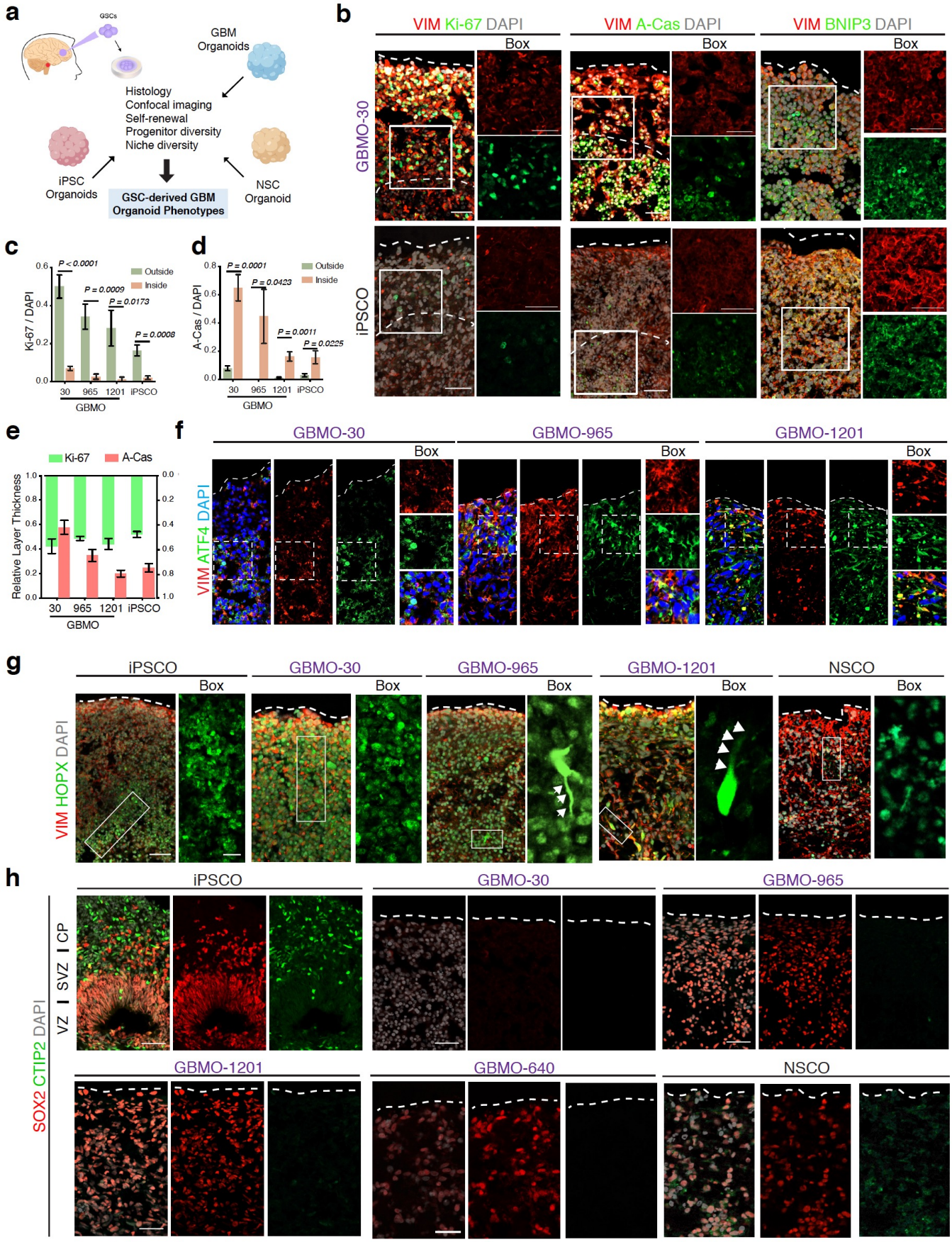
a
GSCs
GBM Organoids
Histology
Confocal imaging
Self-renewal
Progenitor diversity
Niche diversity
iPSC Organoids
NSC Organoid
GSC-derived GBM Organoid Phenotypes
b
VIM Ki-67 DAPI
VIM A-Cas DAPI
VIM BNIP3 DAPI
Box
GBMO-30
iPSCO
c
Ki-67 / DAPI
Outside
Inside
P < 0.0001
P = 0.0009
P = 0.0173
P = 0.0008
30
965
1201
iPSCO
GBMO
d
A-Cas / DAPI
P = 0.0001
P = 0.0423
P = 0.0011
P = 0.0225
e
Ki-67
A-Cas
Relative Layer Thickness
f
GBMO-30
GBMO-965
GBMO-1201
VIM ATF4 DAPI
g
iPSCO
GBMO-30
GBMO-965
GBMO-1201
NSCO
VIM HOPX DAPI
h
VZ
SVZ
CP
SOX2 CTIP2 DAPI
GBMO-1201
GBMO-640

Figure 1

a Characterization of neural progenitors and stem cells markers in GBMOs

iPSCO | GBMO-30 | GBMO-965 | GBMO-1201 | NSCO

REELIN TBR1 DAPI

PAX6 SATB2 DAPI

PAX6 TBR2 DAPI

b Correlation of GBMO progenitors and stem cells markers expression in vivo tissue from TCGA dataset

CTIP2: P < 0.0001, P < 0.0001, P < 0.0001

HOPX: N.S

PAX6: P < 0.01

REELIN: P < 0.0001, P < 0.0001, P < 0.0001

SATB2: P < 0.0001, P < 0.0001, P < 0.0001

SOX2: P < 0.0001, P < 0.0001, P < 0.0001

TBR1: P < 0.0001, P < 0.0001, P < 0.0001

TBR2: P < 0.01

VIM: P < 0.0001, P < 0.0001, P < 0.0001

Cla Mes Pro Nor

c Progenitor diversity

Cerebral Organoid

GBM Organoid

MZ, I, II, III, IV, CP, V, VI, IZ, oSVZ, VZ

REELIN+

SATB2+

CTIP2+

TBR1+

TBR2+

PAX6+

HOPX+

SOX2+

REELIN+ neuron

Layer II, III neuron

SATB2+ neuron

CTIP2+ neuron

TBR1+ neuron

TBR2+ intermediate progenitor

PAX6+ radial glia

HOPX+ outer RG

SOX2+ neuroepithelial progenitor

Figure 2

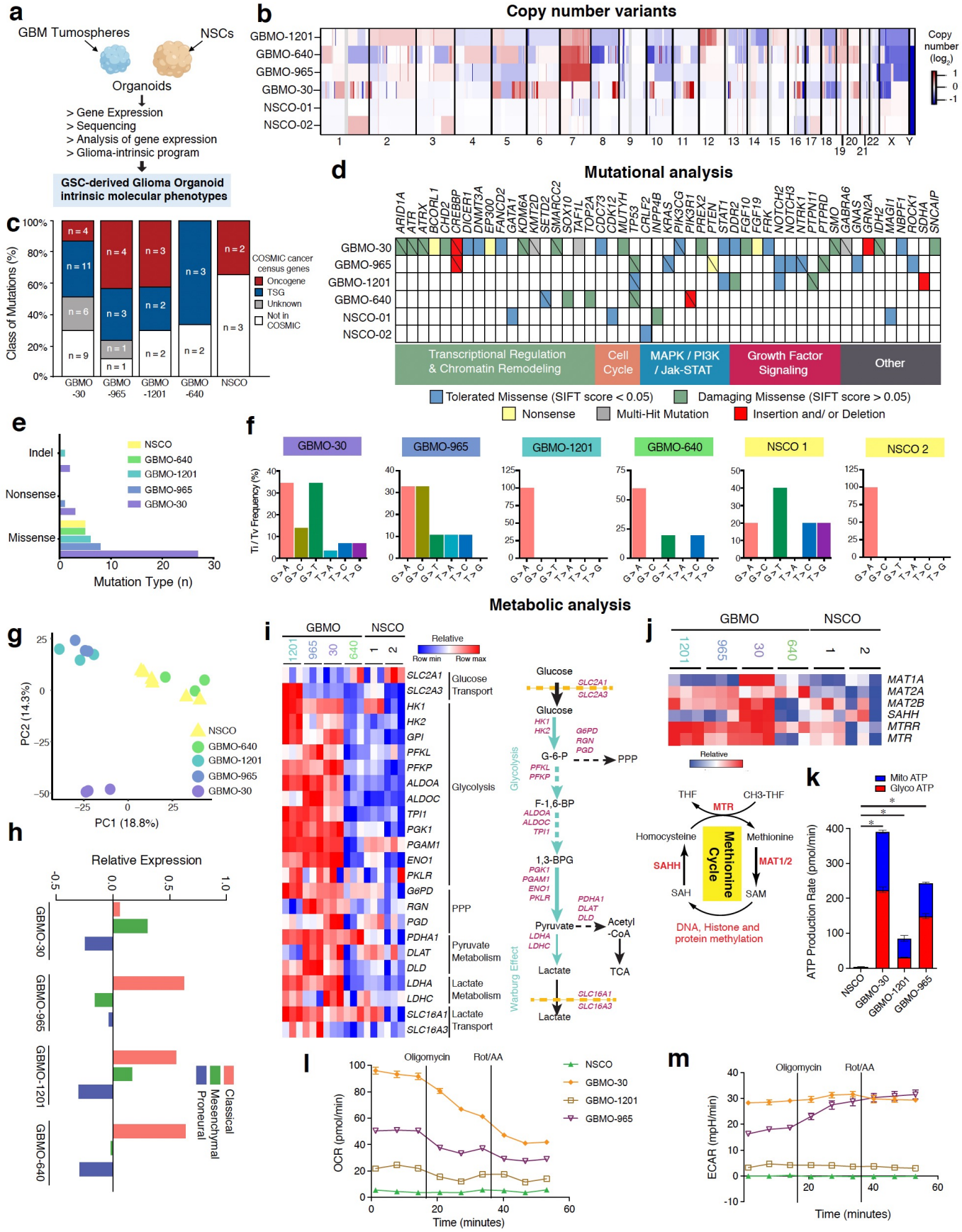
a
GBM Tumospheres
NSCs
Organoids
> Gene Expression
> Sequencing
> Analysis of gene expression
> Glioma-intrinsic program
GSC-derived Glioma Organoid intrinsic molecular phenotypes
b
Copy number variants
GBMO-1201
GBMO-640
GBMO-965
GBMO-30
NSCO-01
NSCO-02
Copy number (log2)
c
Class of Mutations (%)
COSMIC cancer census genes
Oncogene
TSG
Unknown
Not in COSMIC
GBMO -30
GBMO -965
GBMO -1201
GBMO -640
NSCO
d
Mutational analysis
Transcriptional Regulation & Chromatin Remodeling
Cell Cycle
MAPK / PI3K / Jak-STAT
Growth Factor Signaling
Other
Tolerated Missense (SIFT score < 0.05)
Damaging Missense (SIFT score > 0.05)
Nonsense
Multi-Hit Mutation
Insertion and/ or Deletion
e
Indel
Nonsense
Missense
Mutation Type (n)
f
Ti / Tv Frequency (%)
GBMO-30
GBMO-965
GBMO-1201
GBMO-640
NSCO 1
NSCO 2
g
PC2 (14.3%)
PC1 (18.8%)
h
Relative Expression
Classical
Mesenchymal
Proneural
Metabolic analysis
i
Relative
Glucose Transport
Glycolysis
PPP
Pyruvate Metabolism
Lactate Metabolism
Lactate Transport
Warburg Effect
j
MAT1A
MAT2A
MAT2B
SAHH
MTRR
MTR
THF
CH3-THF
Homocysteine
Methionine
SAH
SAM
Methionine Cycle
DNA, Histone and protein methylation
k
Mito ATP
Glyco ATP
ATP Production Rate (pmol/min)
l
Oligomycin
Rot/AA
OCR (pmol/min)
Time (minutes)
m
ECAR (mpH/min)
Time (minutes)

Figure 3

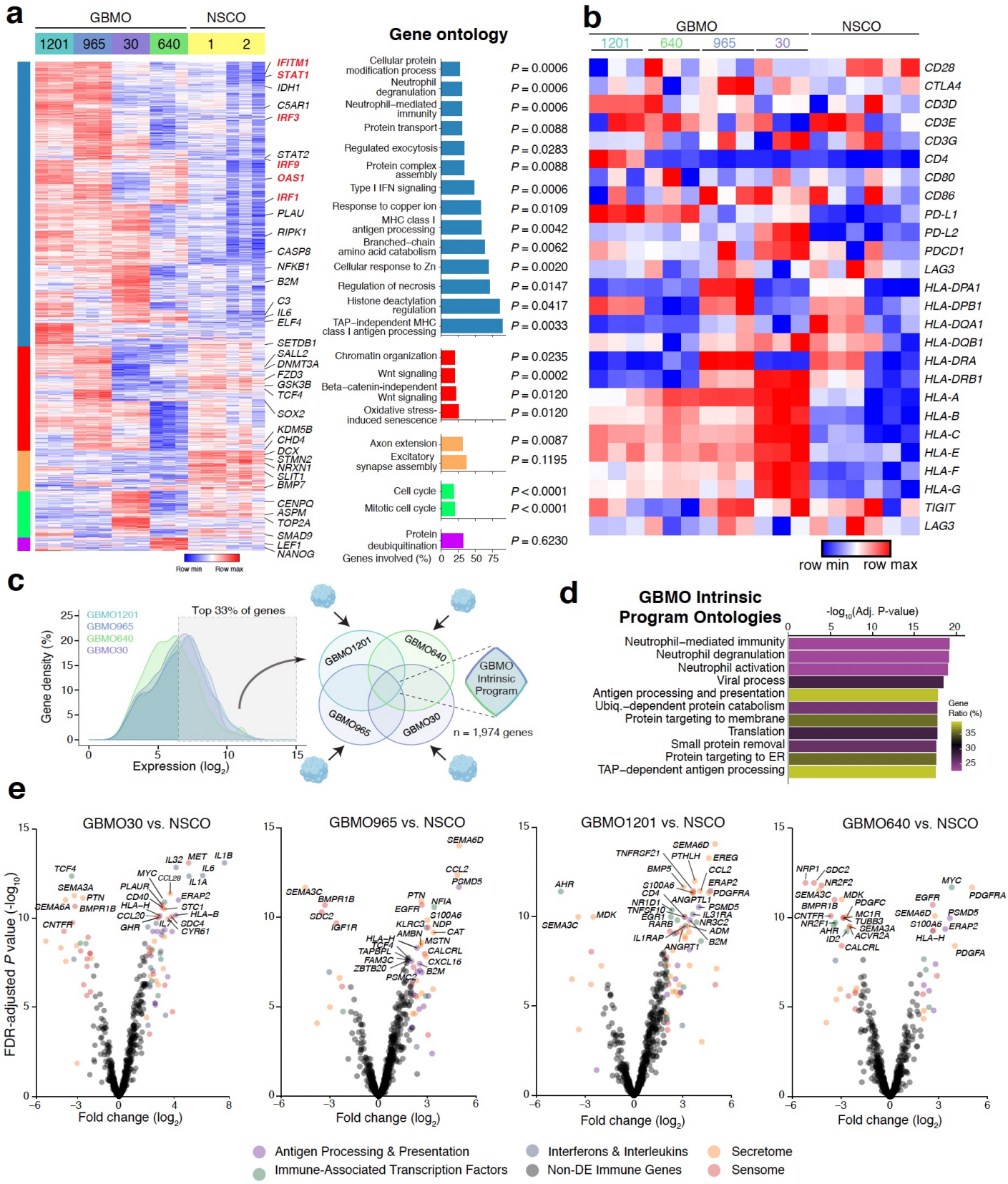
a
GBMO
NSCO
1201
965
30
640
1
2
IFITM1
STAT1
IDH1
C5AR1
IRF3
STAT2
IRF9
OAS1
IRF1
PLAU
RIPK1
CASP8
NFKB1
B2M
C3
IL6
ELF4
SETDB1
SALL2
DNMT3A
FZD3
GSK3B
TCF4
SOX2
KDM5B
CHD4
DCX
STMN2
NRXN1
SLIT1
BMP7
CENPQ
ASPM
TOP2A
SMAD9
LEF1
NANOG
Row min
Row max
Gene ontology
Cellular protein modification process P = 0.0006
Neutrophil degranulation P = 0.0006
Neutrophil–mediated immunity P = 0.0006
Protein transport P = 0.0088
Regulated exocytosis P = 0.0283
Protein complex assembly P = 0.0088
Type I IFN signaling P = 0.0006
Response to copper ion P = 0.0109
MHC class I antigen processing P = 0.0042
Branched–chain amino acid catabolism P = 0.0062
Cellular response to Zn P = 0.0020
Regulation of necrosis P = 0.0147
Histone deactylation regulation P = 0.0417
TAP–independent MHC class I antigen processing P = 0.0033
Chromatin organization P = 0.0235
Wnt signaling P = 0.0002
Beta–catenin-independent Wnt signaling P = 0.0120
Oxidative stress-induced senescence P = 0.0120
Axon extension P = 0.0087
Excitatory synapse assembly P = 0.1195
Cell cycle P < 0.0001
Mitotic cell cycle P < 0.0001
Protein deubiquitination P = 0.6230
Genes involved (%) 0 25 50 75
b
GBMO
NSCO
1201
640
965
30
CD28
CTLA4
CD3D
CD3E
CD3G
CD4
CD80
CD86
PD-L1
PD-L2
PDCD1
LAG3
HLA-DPA1
HLA-DPB1
HLA-DQA1
HLA-DQB1
HLA-DRA
HLA-DRB1
HLA-A
HLA-B
HLA-C
HLA-E
HLA-F
HLA-G
TIGIT
LAG3
row min
row max
c
GBMO1201
GBMO965
GBMO640
GBMO30
Top 33% of genes
Gene density (%)
Expression (log2)
GBMO Intrinsic Program
n = 1,974 genes
d
GBMO Intrinsic Program Ontologies
-log10(Adj. P-value)
Neutrophil–mediated immunity
Neutrophil degranulation
Neutrophil activation
Viral process
Antigen processing and presentation
Ubiq.–dependent protein catabolism
Protein targeting to membrane
Translation
Small protein removal
Protein targeting to ER
TAP–dependent antigen processing
Gene Ratio (%)
e
GBMO30 vs. NSCO
GBMO965 vs. NSCO
GBMO1201 vs. NSCO
GBMO640 vs. NSCO
FDR-adjusted P value (-log10)
Fold change (log2)
Antigen Processing & Presentation
Immune-Associated Transcription Factors
Interferons & Interleukins
Non-DE Immune Genes
Secretome
Sensome

Figure 4

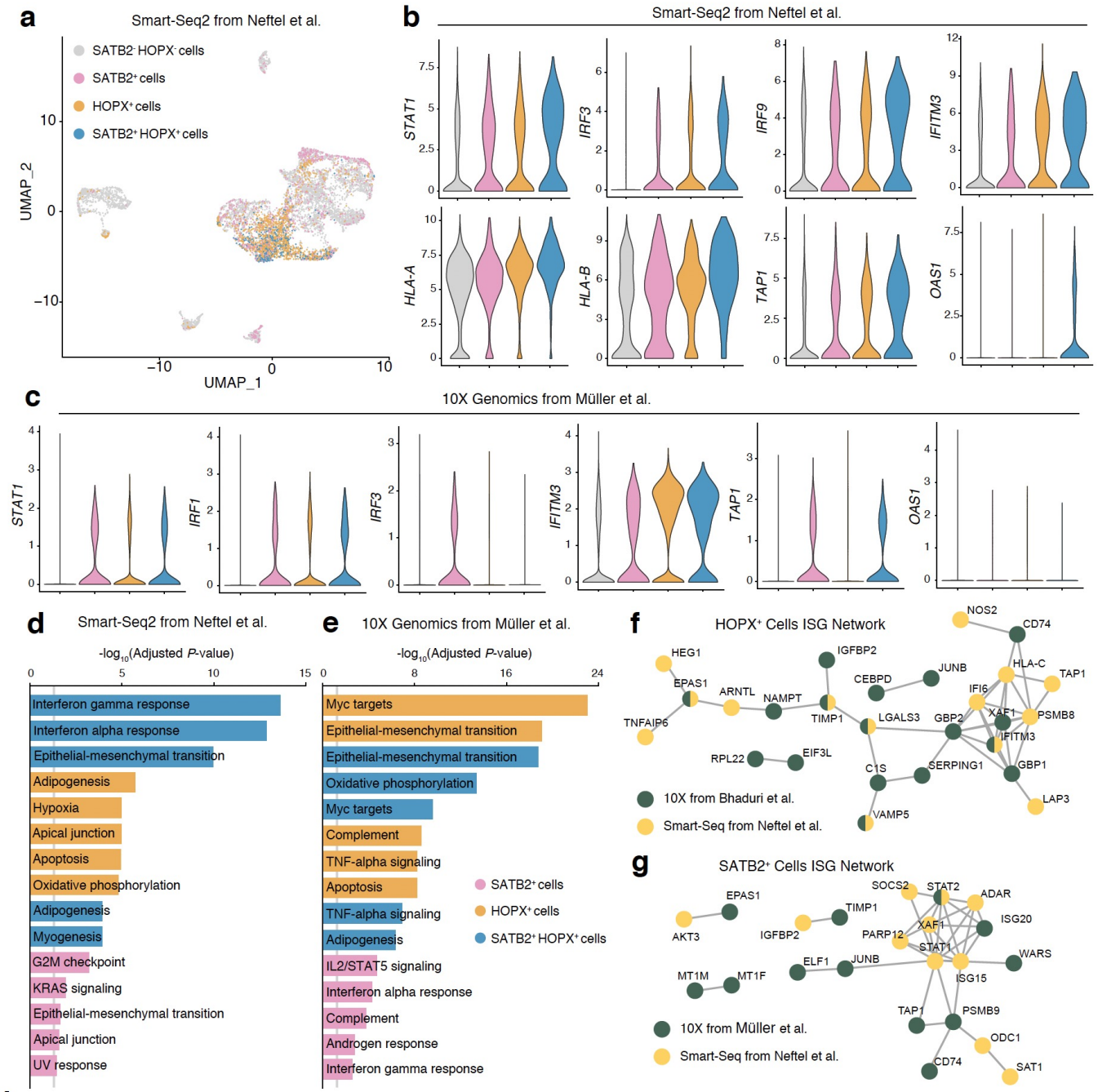
a
Smart-Seq2 from Neftel et al.
SATB2⁻ HOPX⁻ cells
SATB2⁺ cells
HOPX⁺ cells
SATB2⁺ HOPX⁺ cells
UMAP_2
UMAP_1
b
Smart-Seq2 from Neftel et al.
STAT1
IRF3
IRF9
IFITM3
HLA-A
HLA-B
TAP1
OAS1
c
10X Genomics from Müller et al.
STAT1
IRF1
IRF3
IFITM3
TAP1
OAS1
d
Smart-Seq2 from Neftel et al.
-log10(Adjusted P-value)
Interferon gamma response
Interferon alpha response
Epithelial-mesenchymal transition
Adipogenesis
Hypoxia
Apical junction
Apoptosis
Oxidative phosphorylation
Adipogenesis
Myogenesis
G2M checkpoint
KRAS signaling
Epithelial-mesenchymal transition
Apical junction
UV response
e
10X Genomics from Müller et al.
-log10(Adjusted P-value)
Myc targets
Epithelial-mesenchymal transition
Epithelial-mesenchymal transition
Oxidative phosphorylation
Myc targets
Complement
TNF-alpha signaling
Apoptosis
TNF-alpha signaling
Adipogenesis
IL2/STAT5 signaling
Interferon alpha response
Complement
Androgen response
Interferon gamma response
SATB2⁺ cells
HOPX⁺ cells
SATB2⁺ HOPX⁺ cells
f
HOPX⁺ Cells ISG Network
NOS2
CD74
HEG1
IGFBP2
JUNB
HLA-C
TAP1
EPAS1
ARNTL
NAMPT
CEBPD
IFI6
TNFAIP6
TIMP1
LGALS3
GBP2
XAF1
PSMB8
IFITM3
RPL22
EIF3L
C1S
SERPING1
GBP1
LAP3
VAMP5
10X from Bhaduri et al.
Smart-Seq from Neftel et al.
g
SATB2⁺ Cells ISG Network
SOCS2
STAT2
ADAR
EPAS1
TIMP1
ISG20
AKT3
IGFBP2
PARP12
XAF1
STAT1
WARS
ELF1
JUNB
MT1M
MT1F
ISG15
TAP1
PSMB9
ODC1
CD74
SAT1
10X from Müller et al.
Smart-Seq from Neftel et al.
h
DAPI STAT1 SATB2
DAPI STAT1 HOPX
DAPI IFNGR VIM
GBMO-965
Intensity
Distance (μm)
i
DAPI STAT1 SATB2
DAPI STAT1 HOPX
DAPI IFNGR VIM
GBMO-1201
Intensity
Distance (μm)

Figure 5

GSC-derived GBMO model and novel intrinsic phenotypes

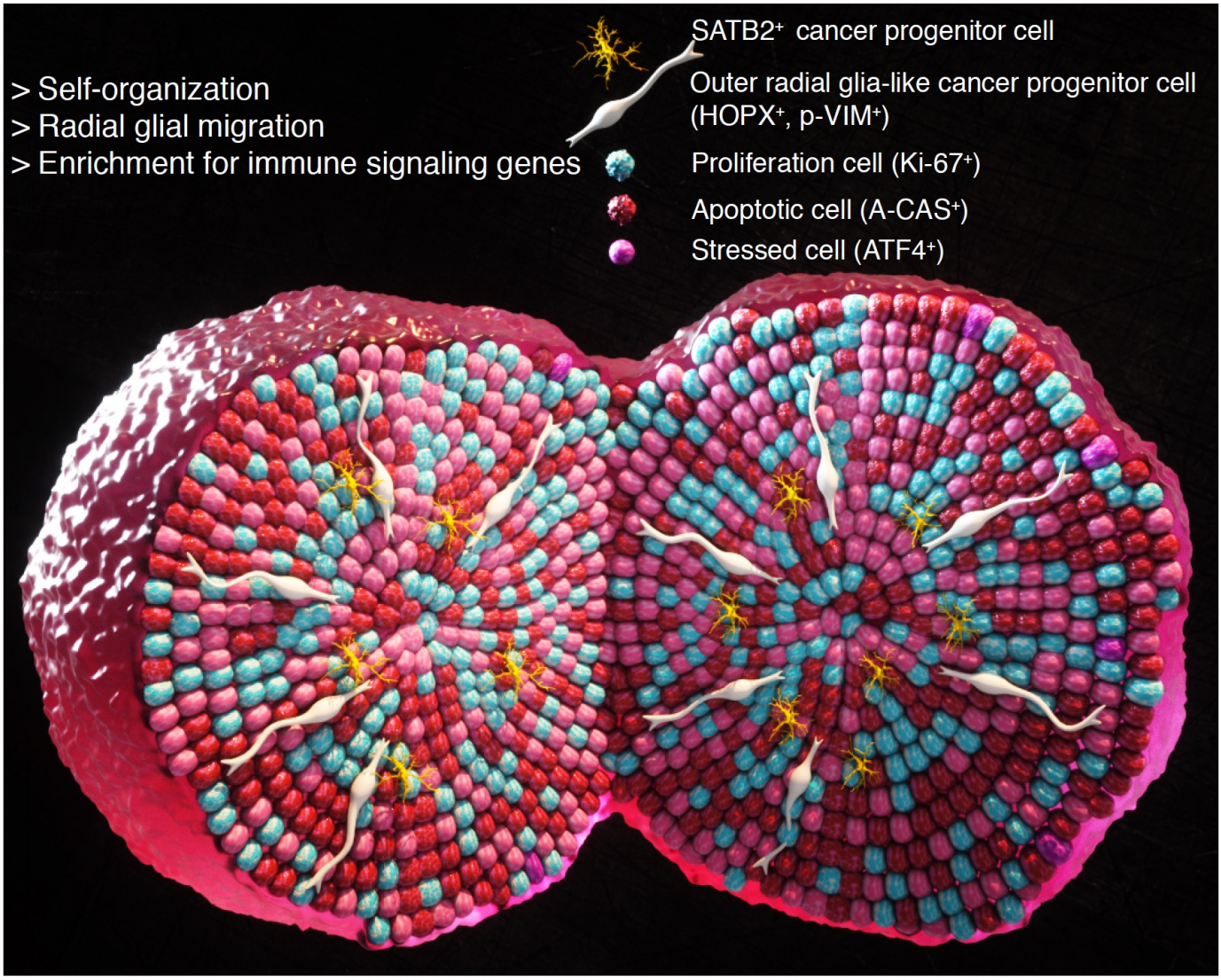

Figure 6

Comparison of GBM tissue and Organoids from the same patient

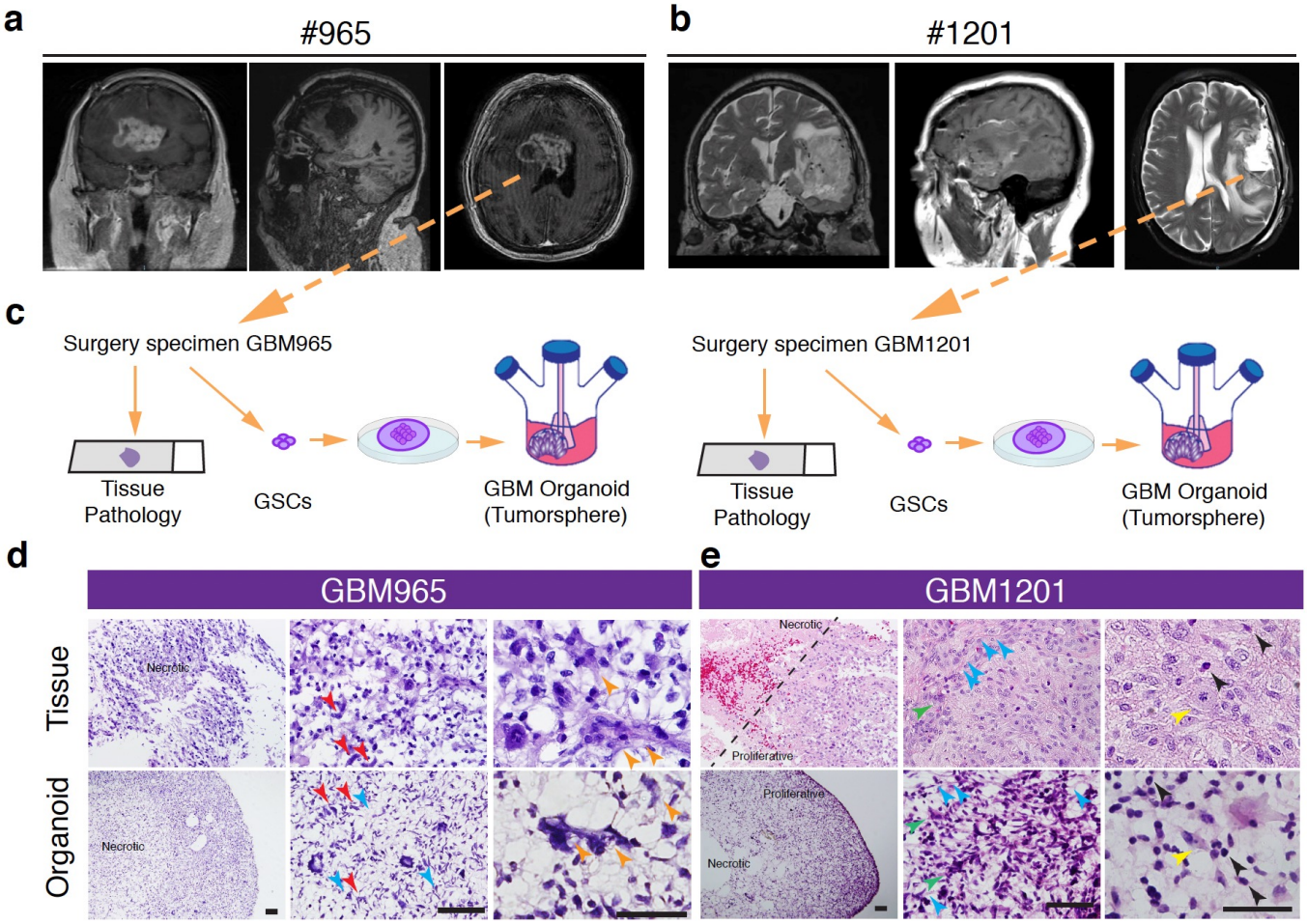

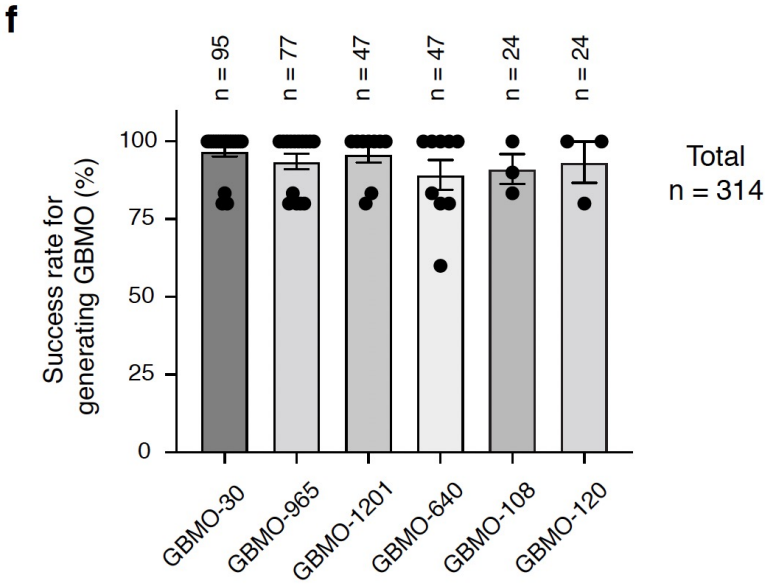

Supplementary Fig. 1

a

Comparison of properties GBM neurospheres vs GBMOs

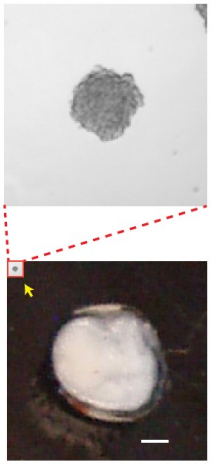

Feature	GBM Neurospheres (GSCs)	GBM Organoid (GBMO)
Size	Diameter: 200 μm	Diameter: 4000 μm (20 Fold)
Layering Organization	Layers Absent Lacks Self-Organization	Layers Present Tissue-Like Self-Organization
Niches	Niches Absent	Apoptotic, Proliferative, & Hypoxic Niches
Self-Renewal	Yes, not after differentiation	Yes, always retained
Transcriptome	N.D.	In Vivo-like Recapitulation

b

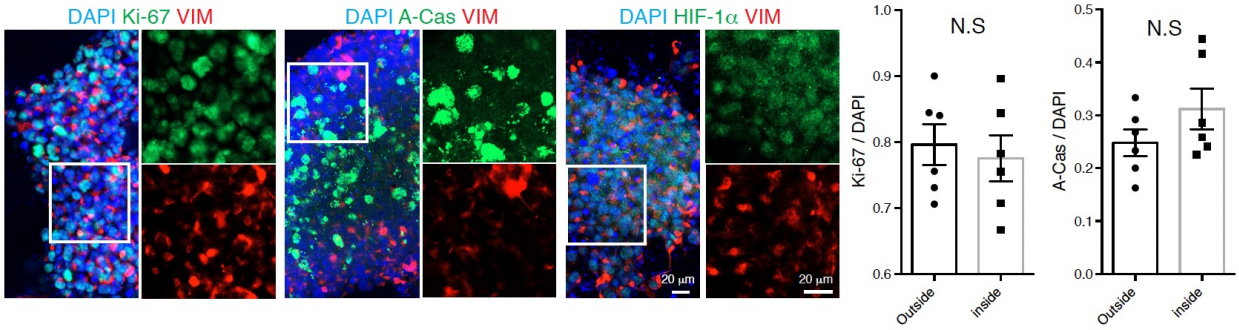

Supplementary Fig. 2

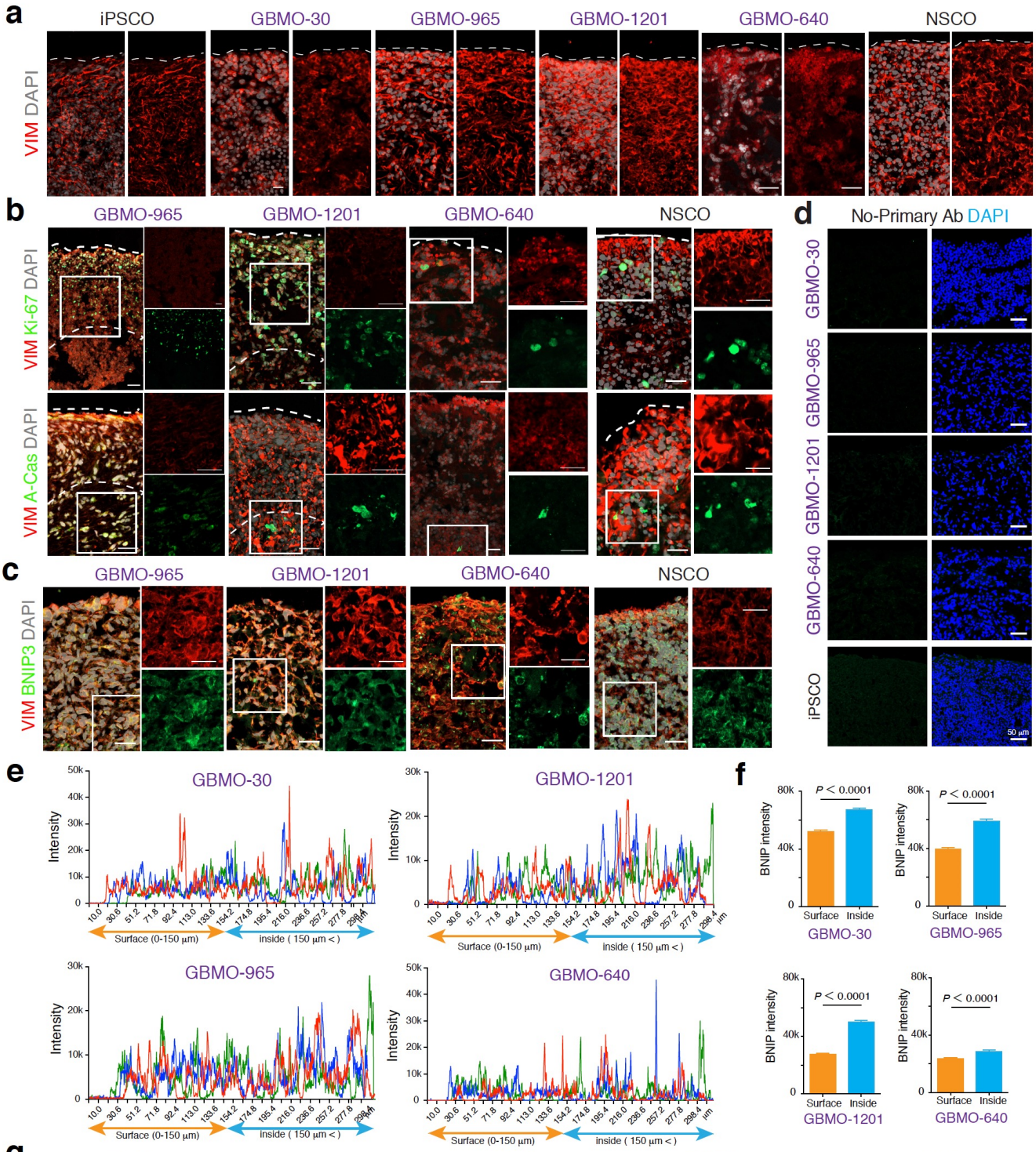

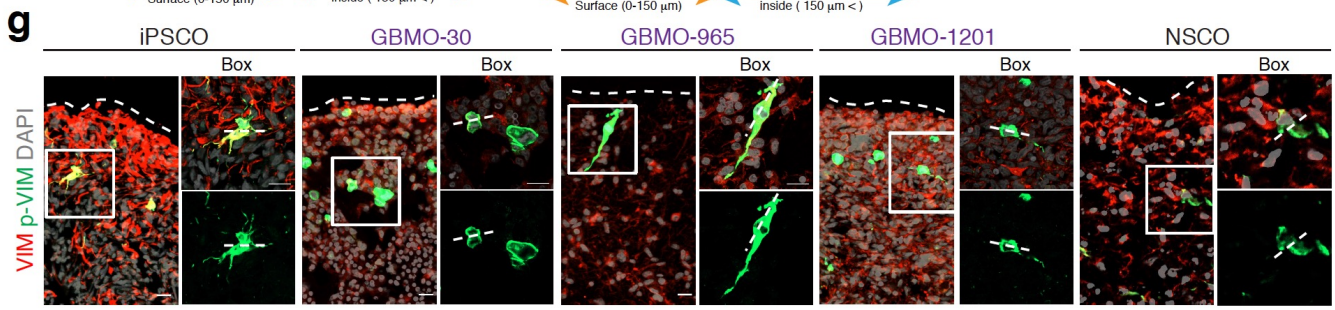

Supplementary Fig. 3

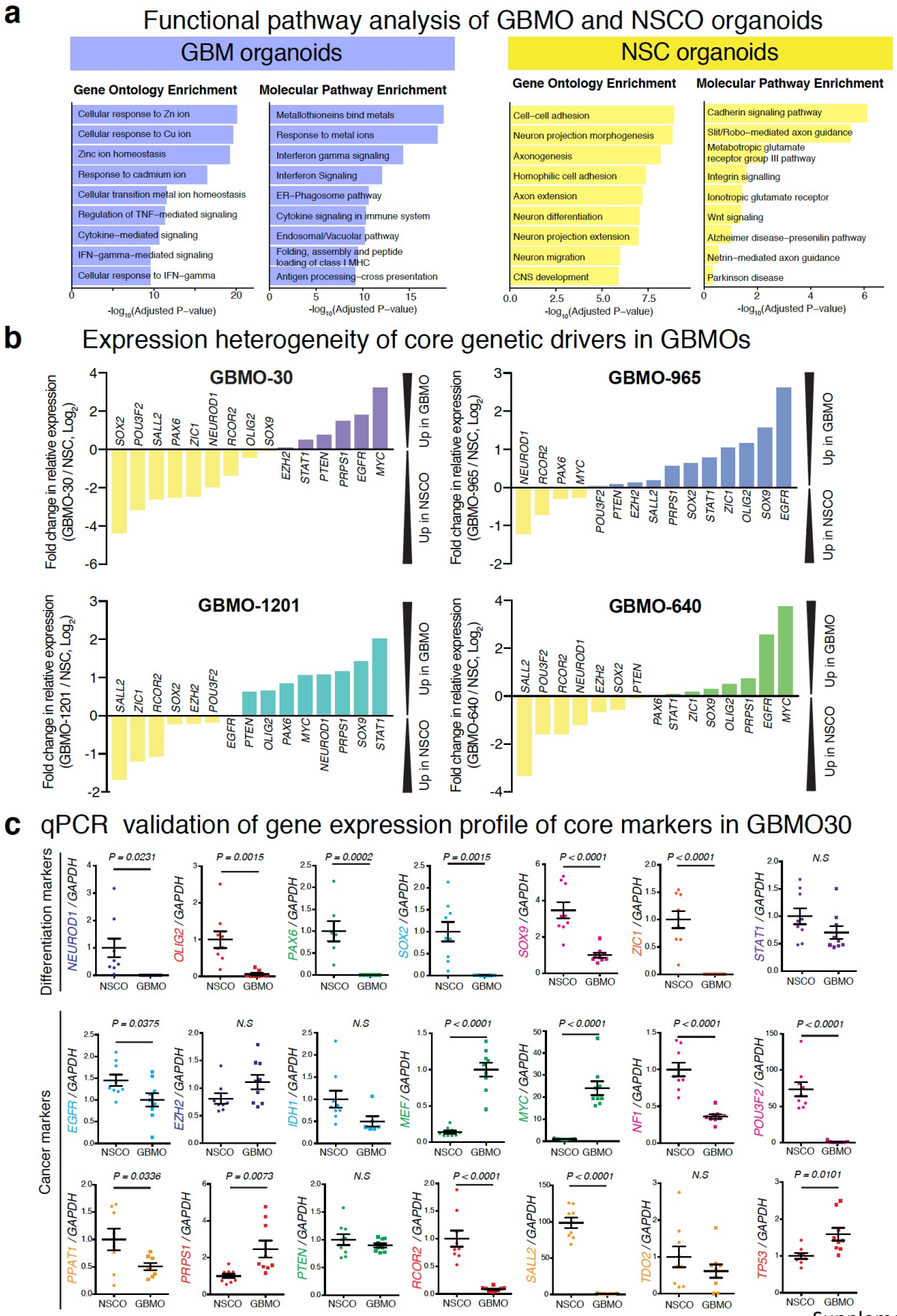

Supplementary Fig. 4

a Microarray of GBMO upregulated gene expression compared to NSCOs

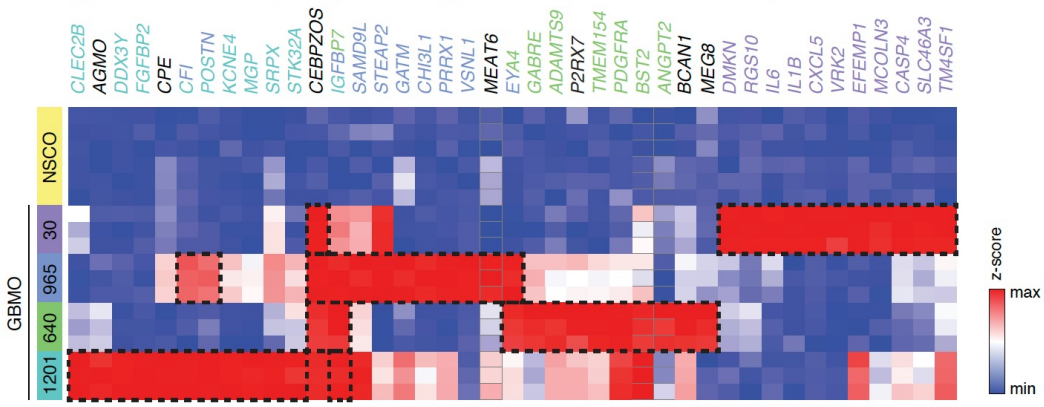

b Correlation of GBMO upregulated gene expression in gliomas

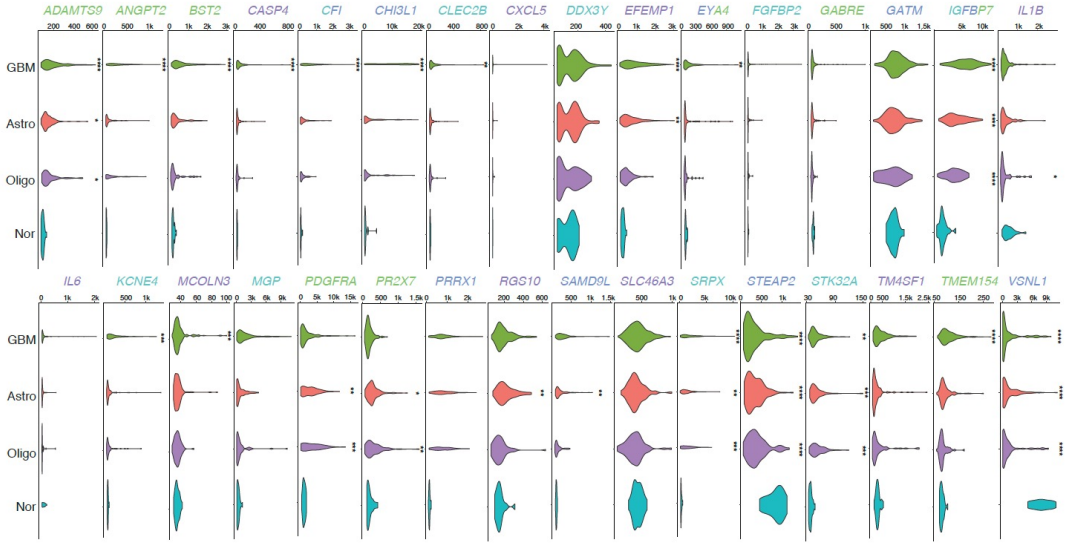

c Correlation of GBMO upregulated gene expression in glioblastomas

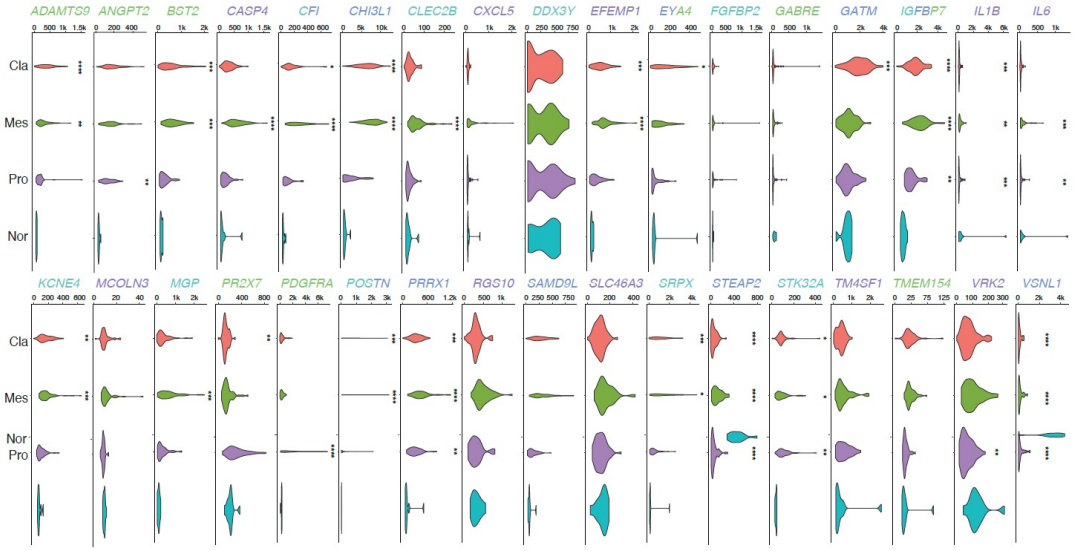

Supplementary Fig. 5

Correlation of differential expression of GBMO genes in in vivo GBM microanatomy by IvyGAP

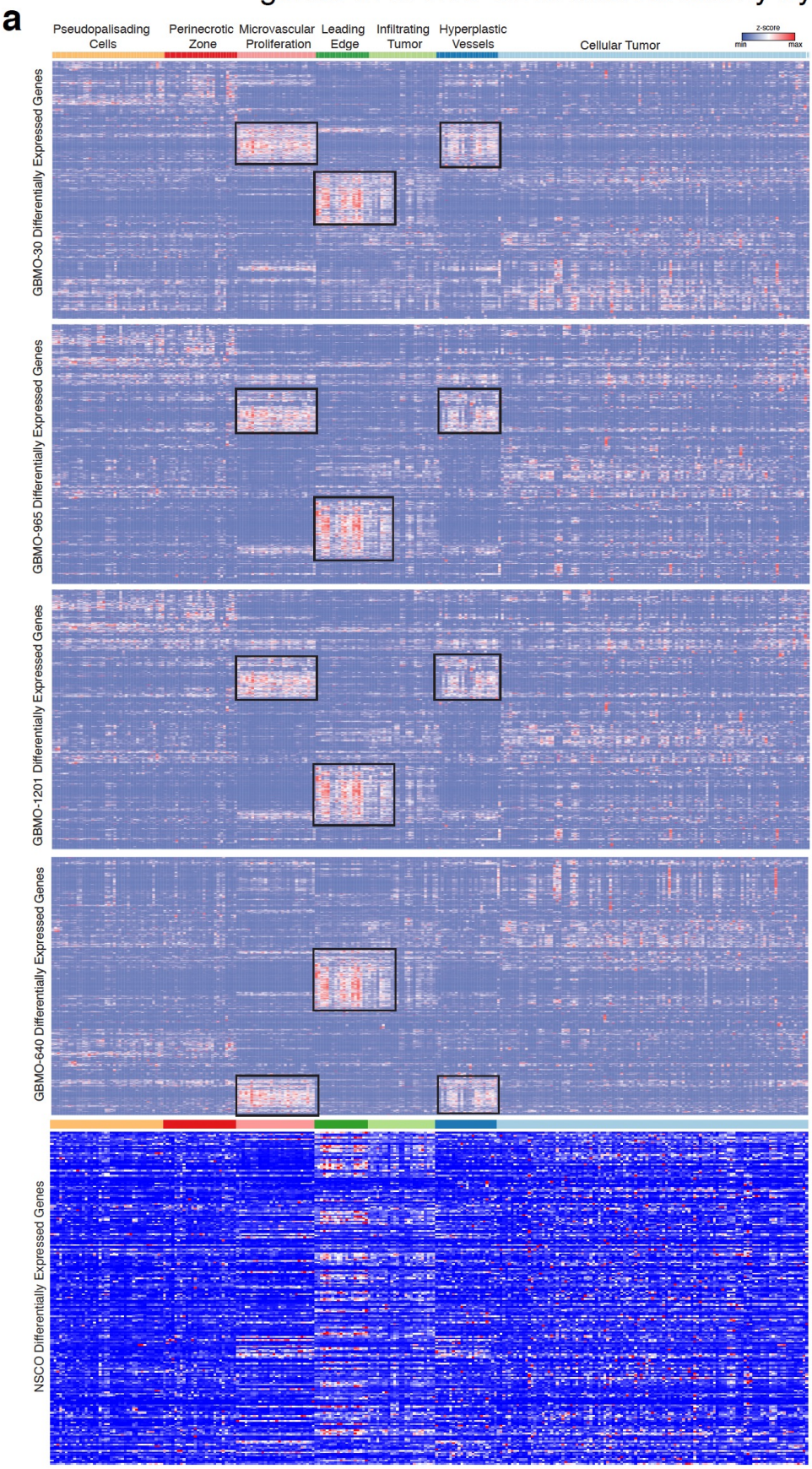

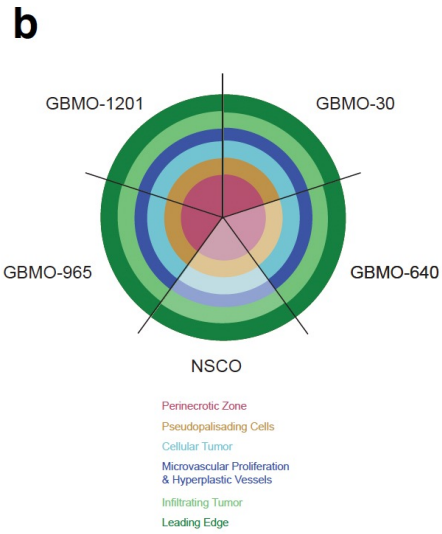

Supplementary Fig. 6

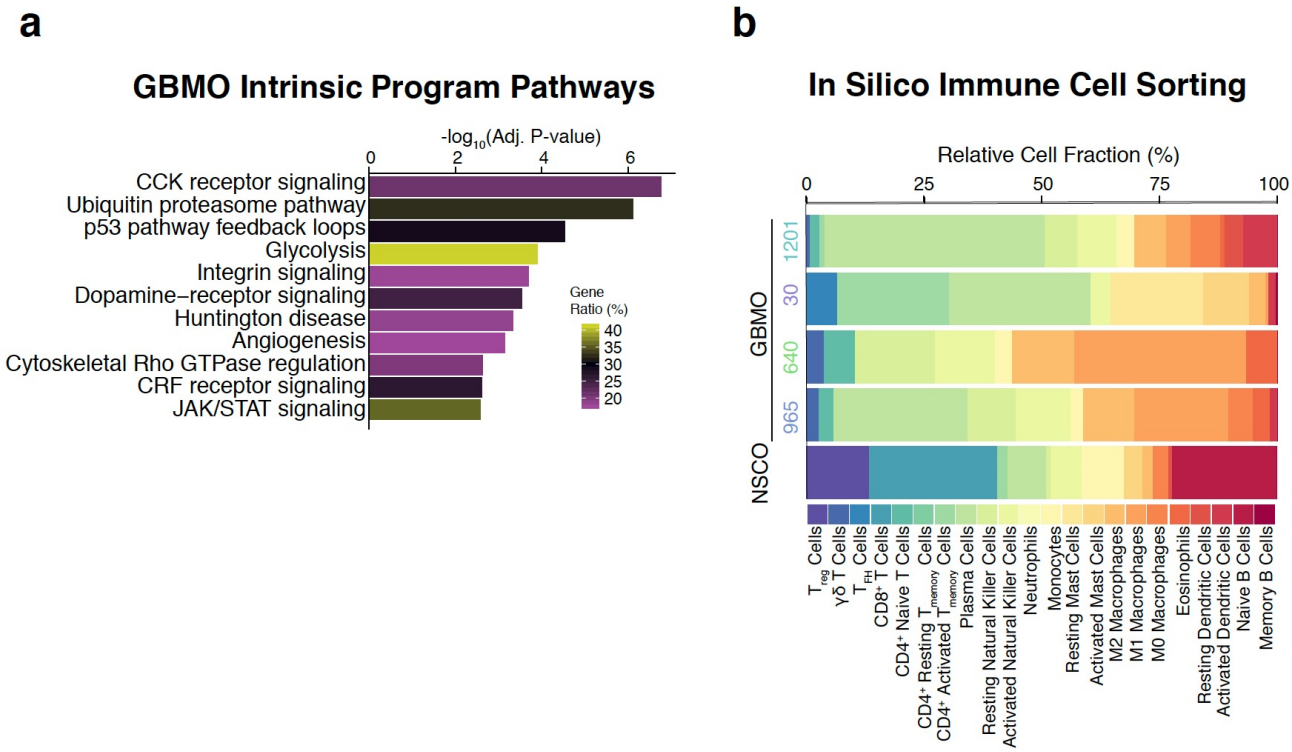

Supplementary Fig. 7

a Validation of absence of absence of immunological cells in GBMOs

GBMO-30 | GBMO-965 | GBMO-1201 | Human GBM

CD4 VIM DAPI

CD8 VIM DAPI

CD68 VIM DAPI

50 µm

b Correlation of glioma intrinsic immune gene expression by single cell dataset

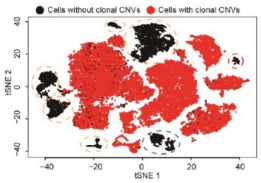

1. Glial-immune preferential expressed in tumor
2. Expressed in glial-immune and bona fide immune cells
3. Expressed only in bona fide immune cells

c Localization of GBMO immune associated gene expression in single cell dataset

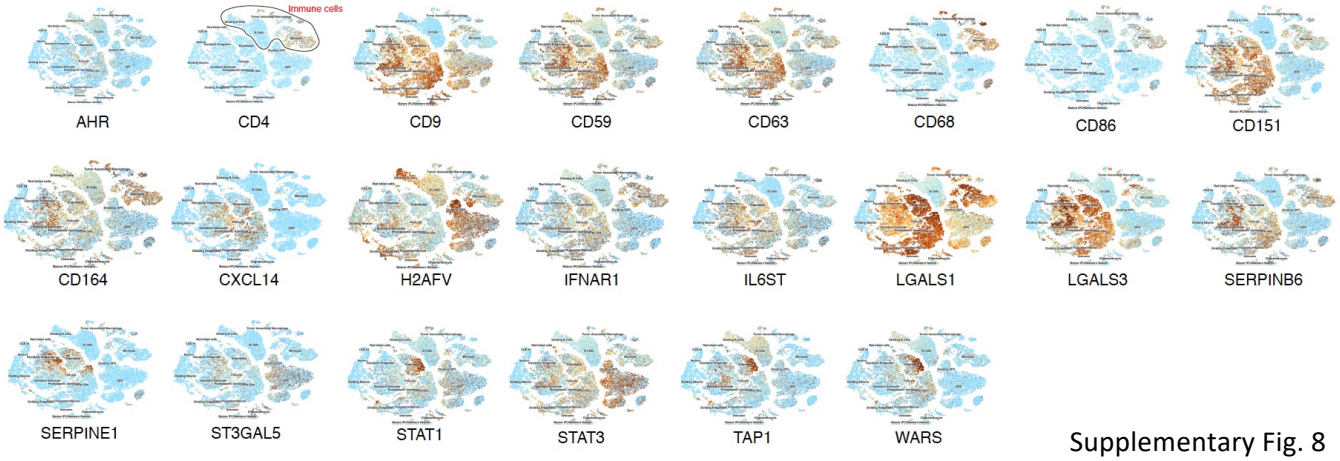

Supplementary Fig. 8

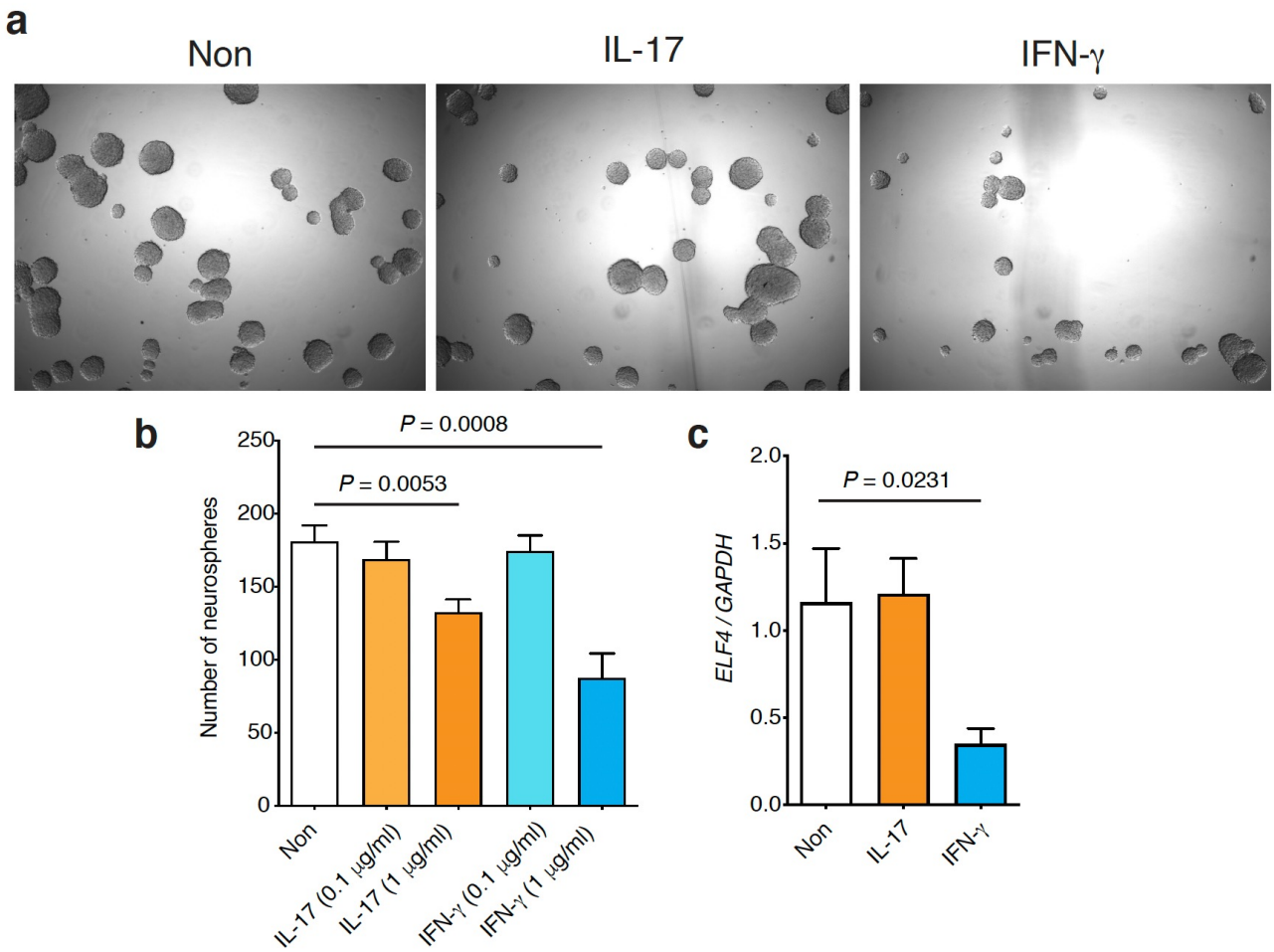

Supplementary Fig. 9

GSC-derived GBMO model and novel intrinsic phenotypes

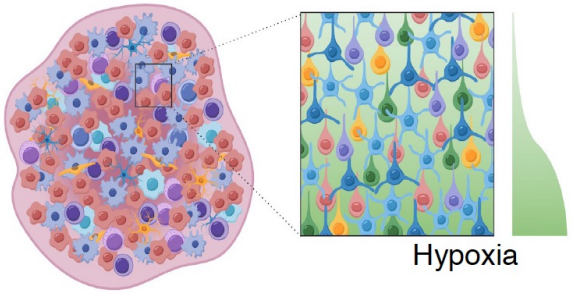

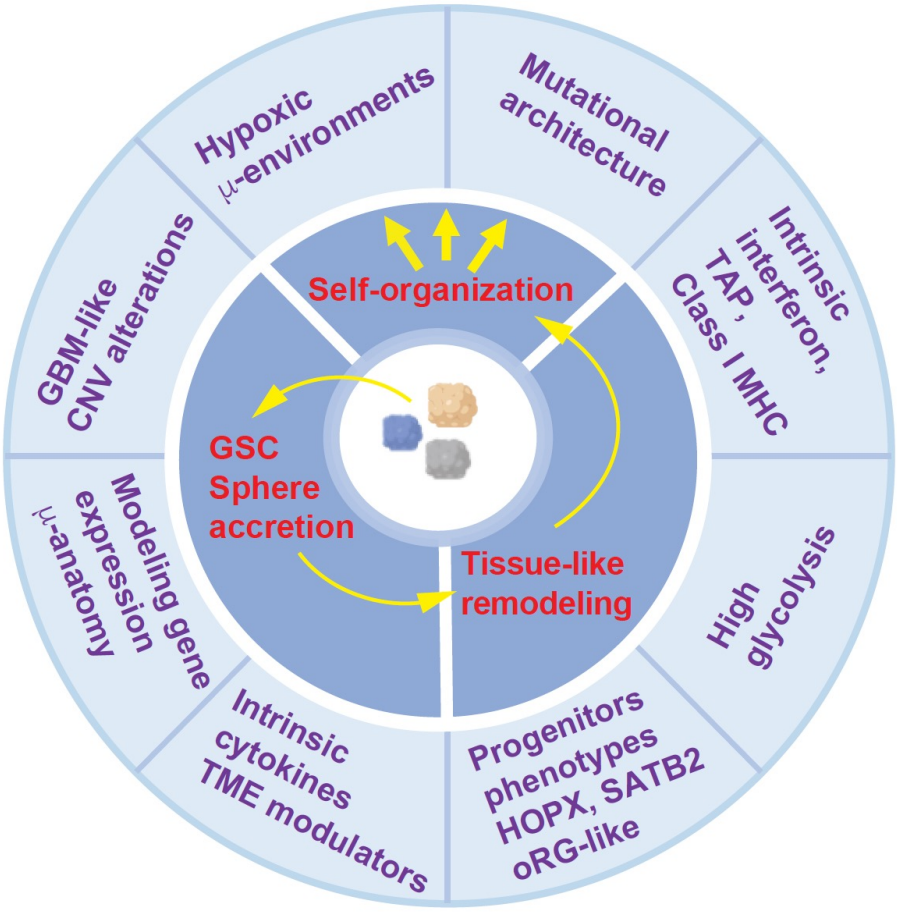

Supplementary Fig. 10